

## Article

# Relationship between Photosynthetic CO<sub>2</sub> Assimilation and Chlorophyll Fluorescence for Winter Wheat under Water Stress

Qianlan Jia <sup>1</sup>, Zhunqiao Liu <sup>2</sup>, Chenhui Guo <sup>1</sup>, Yakai Wang <sup>1</sup>, Jingjing Yang <sup>3,4</sup>, Qiang Yu <sup>2,5</sup>, Jing Wang <sup>2</sup>, Fenli Zheng <sup>2,4</sup> and Xiaoliang Lu <sup>2,\*</sup>

- <sup>1</sup> College of Natural Resources and Environment, Northwest A&F University, Xianyang 712100, China; qianlanjia@nwfau.edu.cn (Q.J.); guochenhui@nwfau.edu.cn (C.G.); wangyakai@nwfau.edu.cn (Y.W.)
- <sup>2</sup> State Key Laboratory of Soil Erosion and Dryland Farming on the Loess Plateau, Northwest A&F University, Xianyang 712100, China; zliu@nwfau.edu.cn (Z.L.); yuq@nwfau.edu.cn (Q.Y.); wangjing.je@163.com (J.W.); flzh@ms.iswc.ac.cn (F.Z.)
- <sup>3</sup> The Research Center of Soil and Water Conservation and Ecological Environment, Chinese Academy of Sciences and Ministry of Education, Xianyang 712100, China; yangjingjing20@mails.ucas.ac.cn
- <sup>4</sup> Institute of Soil and Water Conservation, Chinese Academy of Sciences and Ministry of Water Resources, Xianyang 712100, China
- <sup>5</sup> College of Resources and Environment, University of Chinese Academy of Sciences, Beijing 100049, China
- \* Correspondence: luxiaoliang@nwfau.edu.cn

**Abstract:** Solar-induced chlorophyll fluorescence (SIF) has a high correlation with Gross Primary Production (GPP). However, studies focusing on the impact of drought on the SIF-GPP relationship have had mixed results at various scales, and the mechanisms controlling the dynamics between photosynthesis and fluorescence emission under water stress are not well understood. We developed a leaf-scale measurement system to perform concurrent measurements of active and passive fluorescence, and gas-exchange rates for winter wheat experiencing a one-month progressive drought. Our results confirmed that: (1) shifts in light energy allocation towards decreasing photochemistry (the quantum yields of photochemical quenching in PSII decreased from 0.42 to 0.21 under intermediate light conditions) and increasing fluorescence emissions (the quantum yields of fluorescence increased to 0.062 from 0.024) as drought progressed enhance the degree of nonlinearity of the SIF-GPP relationship, and (2) SIF alone has a limited capacity to track changes in the photosynthetic status of plants under drought conditions. However, by incorporating the water stress factor into a SIF-based mechanistic photosynthesis model, we show that drought-induced variations in a variety of key photosynthetic parameters, including stomatal conductance and photosynthetic CO<sub>2</sub> assimilation, can be accurately estimated using measurements of SIF, photosynthetically active radiation, air temperature, and soil moisture as inputs. Our findings provide the experimental and theoretical foundations necessary for employing SIF mechanistically to estimate plant photosynthetic activity during periods of drought stress.



**Citation:** Jia, Q.; Liu, Z.; Guo, C.; Wang, Y.; Yang, J.; Yu, Q.; Wang, J.; Zheng, F.; Lu, X. Relationship between Photosynthetic CO<sub>2</sub> Assimilation and Chlorophyll Fluorescence for Winter Wheat under Water Stress. *Plants* **2023**, *12*, 3365. <https://doi.org/10.3390/plants12193365>

Academic Editor: Yasutomo Hoshika

Received: 30 August 2023

Revised: 17 September 2023

Accepted: 21 September 2023

Published: 23 September 2023

**Keywords:** photosynthesis model; photosynthetic CO<sub>2</sub> assimilation; pulse-amplitude modulation (PAM); remote sensing; solar-induced chlorophyll fluorescence (SIF); water stress



**Copyright:** © 2023 by the authors. Licensee MDPI, Basel, Switzerland. This article is an open access article distributed under the terms and conditions of the Creative Commons Attribution (CC BY) license (<https://creativecommons.org/licenses/by/4.0/>).

## 1. Introduction

Light energy absorbed by plants is consumed in three competing pathways: photochemistry (photochemical quenching (PQ)), emission of chlorophyll *a* fluorescence (ChlF), and non-photochemical quenching (NPQ) [1]. ChlF emission is the radiative loss of absorbed solar energy in the spectral range from 640 nm to 850 nm, with emission peaks at 685 nm and 740 nm [2]. NPQ is the process by which plants dissipate absorbed photon energy as heat and consists of two components: basal or constitutive heat dissipation (D), and regulated heat dissipation (N). Energy partitioning between these three pathways may be highly dynamic under changing physiological and environmental conditions [3,4].

Thus, by measuring ChlF, one may obtain valuable information on the other two processes, namely, PQ and NPQ. Active ChlF measurements, mainly based on the active pulse-amplitude modulation (PAM) technique [5], have been successfully used to assess changes in photosynthetic machinery and the photosynthetic status of plants [6,7]. However, they are generally applied at the leaf scale because active manipulation of the light environment is required [3]. In recent years, substantial progress has also been made in the passive detection of solar-induced chlorophyll fluorescence (SIF) within solar or telluric absorption features (e.g., O<sub>2</sub>-A at 760 nm), enabling the top-of-canopy (TOC) SIF observations (SIF<sub>toc</sub>) in discrete and narrow wavelength bands to be obtained from remote sensing platforms [8–10]. Many studies have shown that canopy SIF has a strong capacity to predict gross primary productivity (GPP) across a variety of land cover types [4,11–13]. Previous studies have indicated that GPP and SIF have a strong linear relationship, and usually exhibit similar spatial and temporal patterns [9,14,15]. Marrs et al. (2020) [16] suggested that the linear relationship between SIF and GPP at large spatial and temporal scales is the result of a shared driver.

As a consequence of climate change, droughts are expected to increase in frequency, duration and severity in many parts of the world, most notably in Africa, Asia and Central and South America [17], and the drought-induced reduction in crop yields has received widespread attention [18–21]. It is noteworthy that winter wheat is the one of the most important and widely planted staple crops in the world [22], and the normal growth and development of winter wheat can be influenced by drought stress [23–25]. Therefore, a rigorous evaluation of the performance of SIF in detecting early signs of photosynthetic downregulation during droughts is particularly relevant to food security. However, SIF-based studies in this field have reported inconsistent results: satellite or near-ground SIF measurements show remarkable declines during droughts [26–28], but leaf-level SIF/ChlF measurements have a weak and delayed response to water stress [29,30]. Moreover, a key step in estimating GPP from remotely sensed SIF is to parameterize the SIF-GPP relationship with data-driven statistical approaches: a combination of flux-tower measurements and satellite SIF data are used. These approaches do not usually track photosynthesis at regional or global scales, particularly facing the complexity of naturally varying systems. All these controversies and limitations highlight the urgent need to develop a practical approach for estimating GPP. This approach should be based on a mechanistic understanding of the relationship between ChlF and photosynthetic CO<sub>2</sub> assimilation under drought conditions.

To obtain a complete picture of the mechanisms regulating ChlF/SIF emission and photosynthetic CO<sub>2</sub> assimilation under a water deficit, one should not only measure passive ChlF radiance for drought plants, but also, simultaneously, gas exchange and active PAM fluorescence. In this study, we developed a concurrent leaf-level measurement system consisting of a portable gas-exchange system, a PAM instrument, and four high-resolution spectrometers. Using this measurement system, we obtained a variety of key photosynthetic parameters, actively and passively induced ChlF, and the light–response curves of gas exchange for both drought-affected and control plants during a month-long progressive drought experiment. We first show the cascade of decline in these photosynthetic parameters, which include stomatal conductance, net photosynthetic carbon assimilation, electron transport rate, and ChlF emission, in response to water stress. We present the variations in the quantum yields of photochemical quenching in PSII ( $\phi_P$ ), fluorescence ( $\phi_F$ ), and regulated and basal heat dissipation ( $\phi_N$  and  $\phi_D$ ), namely, the probability of an absorbed photon being used in a given pathway, under different drought and light conditions. We pay particular attention to the response of the phase-shift in the  $\phi_F$ - $\phi_P$  relationship to water stress and its implications for interpreting the SIF-GPP relationship. By reformulating the mechanistic light–response (MLR) model [31], we are able to propose a SIF-based mechanistic model to accurately track rapid changes in plant photosynthesis status resulting from drought stress. We discuss (1) the mechanisms regulating the interaction among  $\phi_P$ ,  $\phi_F$ ,  $\phi_N$ , and  $\phi_D$  under different degrees of water stress, (2) the reason why the drought response of satellite SIF observations is more pronounced than that obtained from leaf-level

measurements, and (3) practical considerations regarding the application of the proposed model to large scales.

## 2. Results

### 2.1. The Cascade of Drought-Induced Changes in the Photosynthetic Parameters

The morphology of the plants in the WS treatment significantly changed in response to progressive drought stress over the time course of 1 to 28 days (WS1 to WS28), resulting in the curling (WS7 and 10), yellowing (WS14), drying (WS20) and, ultimately, the death of stems/leaves (WS26) (Figure 1). The  $\theta_{\text{SWC}}$  remained at 19.1% in the control pots but declined in drought-treated pots as the drought intensified. The  $\theta_{\text{SWC}}$  reduction rate was high during the early stages of drought, decreasing by nearly half from 19.1% on WS0 (no stress) to 9.2% on WS9 (Figure 1), with the  $\theta_{\text{SWC}}$  decreasing at a slower rate to 7.3% on day 16 of the drought cycle (WS16) as the drought stress progressed (Figure 1). Subsequently, after the imposition of progressive drought for 18 days (WS18), the  $\theta_{\text{SWC}}$  remained rather stable, only declining by 6.3% by WS28 (Figure 1). The variations in  $\beta_{\text{S}}$  and  $\beta_{\text{B}}$  as the soil dried are provided in the Supporting Information (Figure S1).

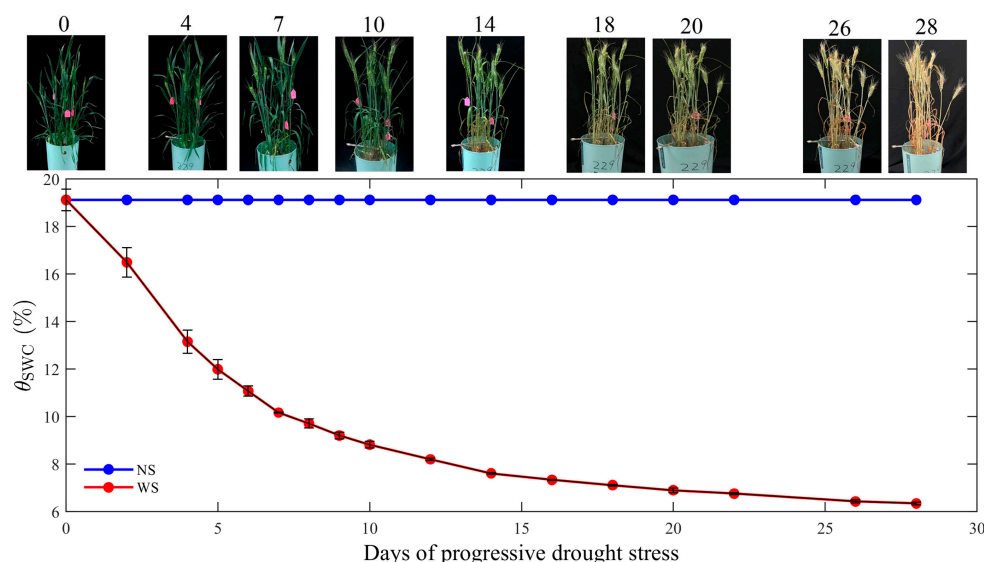


**Figure 1.** Representative images of the water-stressed winter wheat and variation in soil water content ( $\theta_{\text{SWC}}$ , %) for the non-water stress (NS, blue) and water stress (WS, red) treatments under 20 days of progressive drought stress. The numbers above the images represent days after withholding water. Datapoints and error bars represent the mean  $\pm$  standard deviation (SD) of four replicates.

Changes in the light–response curves of  $A_{\text{net}}$ ,  $G_{\text{S}}$ ,  $J_{\text{a\_PAM}}$ , and  $\text{ChlF}_{\text{P\_F}}$  with progressive drought are shown in Figure 2. A strong drought response was observed in  $A_{\text{net}}$ . Increasing water stress diminished both the maximum  $A_{\text{net}}$  value achieved and the irradiance at which this maximum was observed (Figure 2, first row). Light-saturated  $A_{\text{net}}$  decreased from  $24.3 \mu\text{mol m}^{-2} \text{s}^{-1}$  at day 0 (prior to drought treatment) to  $19.1 \mu\text{mol m}^{-2} \text{s}^{-1}$  at day 5, during which time SWC dropped from 19.1% to 12%.  $A_{\text{net}}$  decreased at a greater magnitude subsequently.  $A_{\text{net}}$  in the water-stressed plants fell to near-zero by day ten of the drought. Compared with  $A_{\text{net}}$ ,  $G_{\text{S}}$  showed an even more pronounced drought response (Figure 2, second row). Light-saturated  $G_{\text{S}}$  dropped by more than 60%, or from  $0.54 \text{ mol m}^{-2} \text{s}^{-1}$  to  $0.21 \text{ mol m}^{-2} \text{s}^{-1}$ , after only 5 days of drought, and the stomata almost completely closed on the 8th day of treatment (i.e.,  $G_{\text{S}} \approx 0$  during each light regime). Drought stress had a relatively smaller effect on the electron transport rate (Figure 2, third row). The maximum  $J_{\text{a\_PAM}}$  reached  $120.2 \mu\text{mol m}^{-2} \text{s}^{-1}$  after 5 days of water stress, or about 85% of the corresponding value at the beginning of the experiment. Over 10 days of drought, the maximum  $J_{\text{a\_PAM}}$  still accounted for about 30% of that at WS0, while both  $A_{\text{net}}$  and

$G_s$  approached 0. The fluorescence response occurred much later, and was much smaller, than the responses of  $A_{net}$ ,  $G_s$ , and  $J_{a\_PAM}$  (Figure 2, bottom row); there were only small variations in the light–response curve of  $ChlF_{P\_F}$  during the first 12 days into the drought. We found that absorbed PAR in the water-stressed plants remained almost unchanged during this 12-day period of water stress development (Figure S2), which may explain the weak drought response in the fluorescence emission. In fact, the  $ChlF_{P\_F}$  value of the water-stressed plants maintained a fairly high level of  $ChlF_{P\_F}$  after two weeks of water stress, and was still detectable at WS26 (Figure S3).

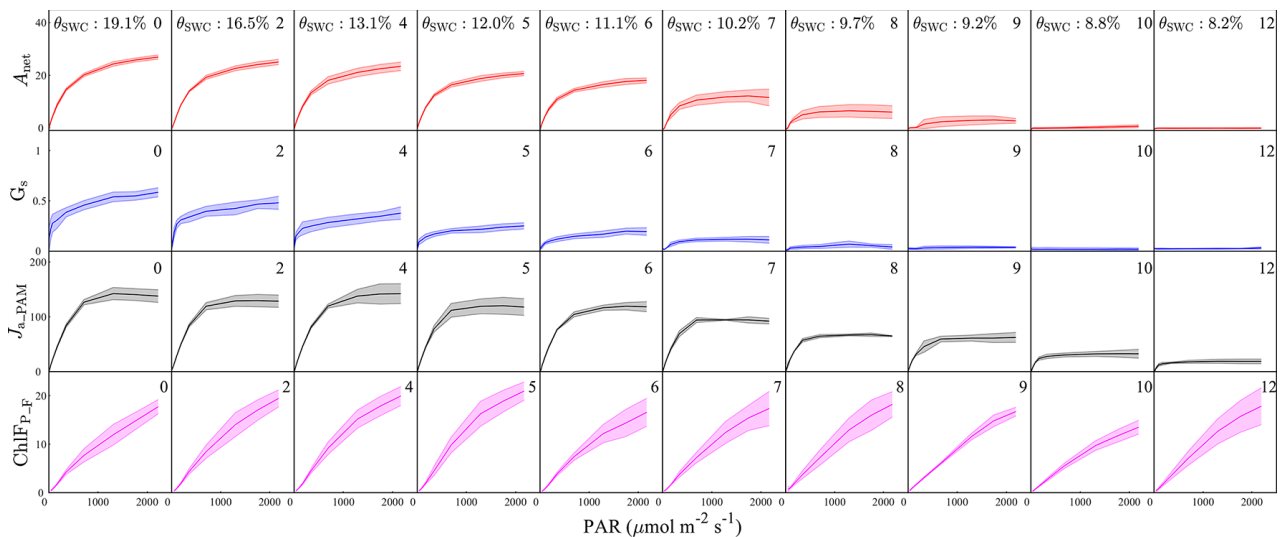


**Figure 2.** The impact of progressive drought stress on the responses of net photosynthetic carbon assimilation ( $A_{net}$ ,  $\mu\text{mol m}^{-2} \text{s}^{-1}$ ), stomatal conductance ( $G_s$ ,  $\text{mol m}^{-2} \text{s}^{-1}$ ), actual rate of electron transport ( $J_{a\_PAM}$ ,  $\mu\text{mol m}^{-2} \text{s}^{-1}$ ), and full-band chlorophyll fluorescence emission at the photosystem level ( $ChlF_{P\_F}$ ,  $\mu\text{mol m}^{-2} \text{s}^{-1}$ ) to changing light intensity. The number in the upper right corner of each plot is the number of days of progressive drought stress. The soil water content ( $\theta_{SWC}$ , %) is also indicated. The solid lines represent the mean, and the shaded areas are  $\pm 1$  standard deviation, of four replicates.  $A_{net}$  and  $G_s$  are measured by the gas-exchange system.

## 2.2. Drought-Induced Changes in the Photosynthesis–Fluorescence Relationship

We compared changes in  $ChlF_{P\_F}$  during the light–response curves against the  $A_{net}$  of individual samples in the WS treatment under different water stress conditions: zero ( $\theta_{SWC} = 19.1\%$ ), moderate ( $\theta_{SWC} = 12.0\%$ ), and high ( $\theta_{SWC} = 9.7\%$ ), which occurred at WS0, WS5, and WS8, respectively (Figure 3). Water stress regulated both the saturation levels of  $A_{net}$  and how the saturation level was approached as  $ChlF_{P\_F}$  increased. Under no drought stress,  $A_{net}$  showed an initial linear increase with increasing  $ChlF_{P\_F}$  and reached around  $25 \mu\text{mol m}^{-2} \text{s}^{-1}$  when  $ChlF_{P\_F} = 10 \mu\text{mol m}^{-2} \text{s}^{-1}$ , after which it largely leveled off with a further increase in  $ChlF_{P\_F}$  (Figure 3). As water stress increased,  $A_{net}$  tended to increase less steeply and reached a plateau at a lower  $ChlF_{P\_F}$ . For the plants exposed to moderate drought, for example,  $A_{net}$  started to remain stable at nearly  $17 \mu\text{mol m}^{-2} \text{s}^{-1}$  when  $ChlF_{P\_F} > 6 \mu\text{mol m}^{-2} \text{s}^{-1}$  (Figure 3). At severe water stress levels, the dynamic of  $ChlF_{P\_F}$  was relatively less affected;  $ChlF_{P\_F}$  still increased from 0 to  $20 \mu\text{mol m}^{-2} \text{s}^{-1}$ , with PAR ranging from 0 to  $2100 \mu\text{mol m}^{-2} \text{s}^{-1}$ . However,  $A_{net}$  started to saturate even when  $ChlF_{P\_F} > 4 \mu\text{mol m}^{-2} \text{s}^{-1}$  and remained less than  $8 \mu\text{mol m}^{-2} \text{s}^{-1}$  for the complete light–response curve (Figure 3).

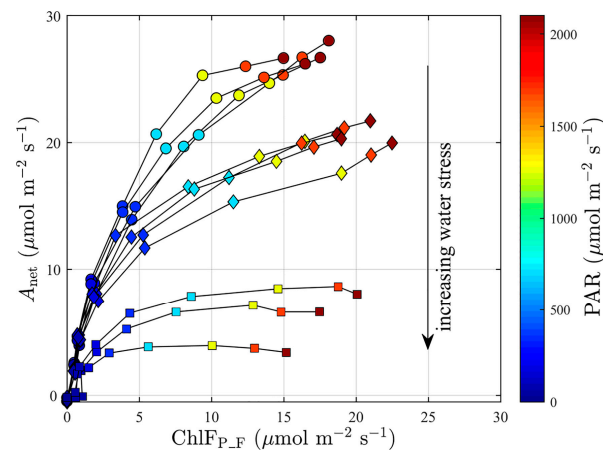


**Figure 3.** Relationships of net photosynthetic carbon assimilation ( $A_{net}$ ,  $\mu\text{mol m}^{-2} \text{s}^{-1}$ ) with full-band chlorophyll fluorescence emission at the photosystem level ( $\text{ChlF}_{P\_F}$ ,  $\mu\text{mol m}^{-2} \text{s}^{-1}$ ). Individual light-response curves are indicated by the black lines connecting measurements obtained at increasing light levels (0–2100  $\mu\text{mol m}^{-2} \text{s}^{-1}$ ). Circles indicate no water stress ( $\theta_{\text{SWC}} = 19.1\%$ ), diamonds represent moderate water stress ( $\theta_{\text{SWC}} = 12.0\%$ ), and squares indicate plants under high water stress ( $\theta_{\text{SWC}} = 9.7\%$ ). The number of light-response curves under high water stress was smaller than those under no water stress and moderate water stress due to human error, leading to unrealistic values in the measurements.  $A_{net}$  is obtained from the gas-exchange system.

### 2.3. The Variations in the Mechanisms Linking Photosynthesis and Fluorescence under Drought

The increasing nonlinearity in the relationship between  $A_{net}$  and  $\text{ChlF}_{P\_F}$  (Figure 3) suggests that water stress causes shifts in the allocation of absorbed light energy dissipation pathways. At the beginning of the experiment (WS0, non-stress),  $\phi_P$  showed an inverse correlation with PAR and exhibited less sensitivity to PAR with increased light levels (Figure 4). The trade-offs between these yields appear to be governed by the complementarity between PQ and NPQ:  $\phi_N$  increased with increased PAR, and  $\phi_P + \phi_N \approx 0.8$  (Figure 4). In contrast,  $\phi_D$  and  $\phi_F$  had a muted sensitivity to changes in PAR: both of them showed a slight increasing trend at low light levels, and a decreasing trend at intermediate or high light levels (Figure 4).

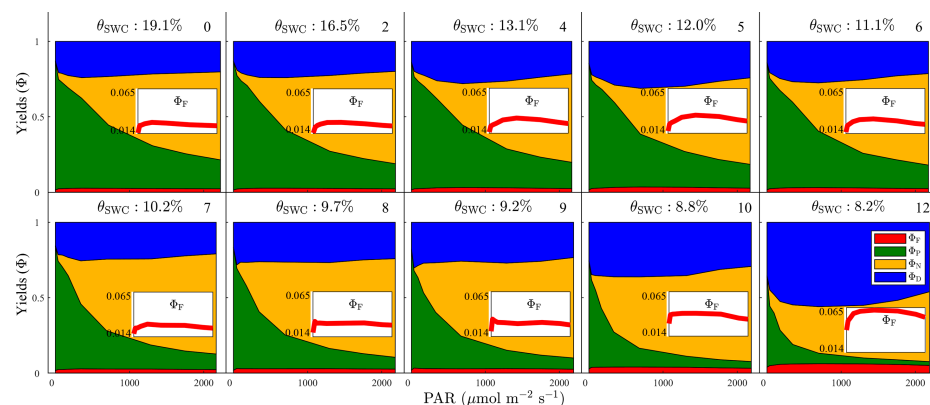


**Figure 4.** Light-response curves of the quantum yields ( $\phi$ ) for the four different pathways during progressive drought stress: fluorescence ( $\phi_F$ , red), photosynthesis ( $\phi_P$ , green), regulated heat dissipation ( $\phi_N$ , yellow), and basal heat dissipation ( $\phi_D$ , blue). The number in the upper right corner of each plot indicates the day of progressive drought stress. The soil water content ( $\theta_{\text{SWC}}$ , %) of progressive drought stress treatment is also given. The inset panel illustrates the pattern of  $\phi_F$  under changing light intensity. The quantum yields ( $\phi$ ) for the four different pathways are obtained from PAM measurements.

During the first five days after imposing water treatment (WS1 to WS5), when  $\theta_{\text{SWC}}$  decreased from 19.1% to 12.0%, the light-response curves of  $\phi_P$ ,  $\phi_N$ ,  $\phi_D$  and  $\phi_F$  showed a weak response to drought under low PAR conditions. For example,  $\phi_P$  taken at  $\text{PAR} = 180 \mu\text{mol m}^{-2} \text{s}^{-1}$  decreased slightly from 0.63 to 0.61. However, a further reduction in  $\phi_P$  occurred at higher PAR levels; for instance,  $\phi_P$  at  $\text{PAR} = 700 \mu\text{mol m}^{-2} \text{s}^{-1}$  decreased from 0.42 to 0.36 (Figure 4).  $\phi_N$  showed a small increasing trend during each light regime, with a larger magnitude under intermediate and high light conditions (Figure 4). Both  $\phi_D$  and  $\phi_F$  increased over the entire light-response curve (Figure 4).

From the 6th to the 8th day of treatment (WS6 to WS8), the variations in these four yields were still relatively limited when  $\text{PAR} \leq 700 \mu\text{mol m}^{-2} \text{s}^{-1}$ . However,  $\phi_P$  showed a significant decline at high PAR values: at WS8,  $\phi_P$  decreased to 0.13, 0.10, and 0.07 at 1300, 1700, and 2100  $\mu\text{mol m}^{-2} \text{s}^{-1}$ , respectively (Figure 4). NPQ still remained complementary to PQ:  $\phi_{\text{NPQ}}$  increased to 0.51, 0.62, 0.65 for these three PAR regimes (Figure 4). Their net effect on  $\phi_D$  and  $\phi_F$  was diminished; the light responses of  $\phi_D$  remained fairly unchanged and  $\phi_F$  showed a small decreasing trend (Figure 4).

During the period between 9 and 12 days (WS9 to WS12), after withholding water, when  $\theta_{\text{SWC}}$  dropped below 9.0%,  $\phi_P$  decreased rapidly with increasing PAR, and this drop grew steeper as water stress developed (Figure 4). In other words, additional water stress increased the degree of nonlinearity in the relationship between  $\phi_P$  and PAR. We also found that a severe water deficit may reduce the complementarity between PQ and NPQ;  $\phi_N$  also showed a clear decreasing trend throughout the light-response curves (Figure 4). As these four pathways compete for absorbed energy, both  $\phi_D$  and  $\phi_F$  showed a clear increase: the maximum  $\phi_D$  and  $\phi_F$  reached 0.57 and 0.03, respectively, on the 12th day of treatment (Figure 4).

#### 2.4. The Phase-Shift in the Relationship between Photochemical and Fluorescence Yields

The nonlinear relationship between  $\phi_F$  and  $\phi_P$  physiologically regulates the asymptotic behavior of the link between fluorescence and photosynthesis, that is, a positive or negative SIF-GPP relationship [32,33]. Similarly to Maguire et al. [34], we fitted a polynomial model to the relationship between  $\phi_F$  and  $\phi_P$ , and the breakpoint was identified as the value of  $\phi_P$  where the slope of polynomial shifted from positive to negative (Figure 5). This breakpoint separates the relationship between  $\phi_F$  and  $\phi_P$  into two parts [3]: (1)  $\phi_F$  is proportional to  $\phi_P$  under low  $\phi_P$  (i.e., high light, 'NPQ phase'), and (2)  $\phi_F$  is inversely proportional to  $\phi_P$  under high  $\phi_P$  (i.e., low light, 'PQ phase').

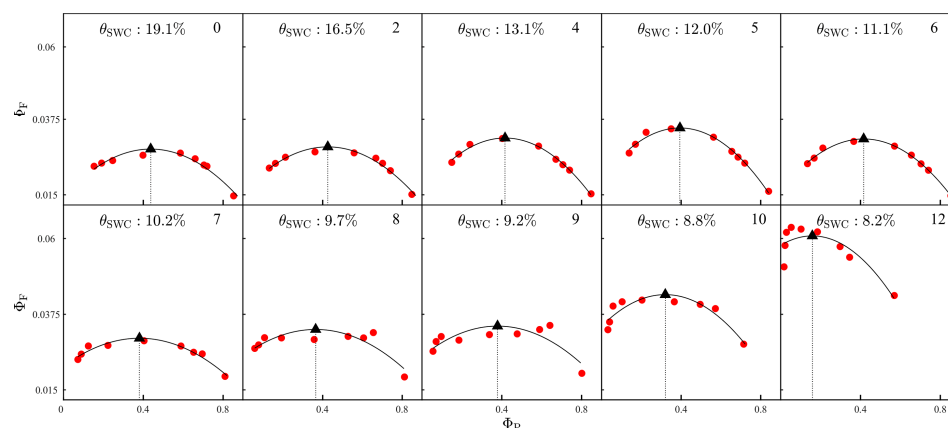


**Figure 5.** Relationships between the quantum yields of fluorescence ( $\phi_F$ ) and photochemical quenching in PSII (red circle) during the progressive onset of drought stress. Polynomial models were used to fit all relationships (black solid lines). Breakpoints (black triangles) are the value of  $\phi_P$  at which the slope of the  $\phi_P$ - $\phi_F$  relationship changes sign.

At WS0, the breakpoint was located at  $\phi_P = 0.46$ .  $\phi_F$  was positively correlated with  $\phi_P$  when  $\phi_P \leq 0.46$ , and they were negatively correlated when  $\phi_P > 0.46$  (Figure 5). The imposition of progressive drought for 5 days (WS1 to WS5) made the phase-shift in the  $\phi_P$ - $\phi_F$  relationship occur at a lower  $\phi_P$ ; the value of  $\phi_P$  at the breakpoints dropped from 0.46 to 0.37 (Figure 5). However, the breakpoints showed no clear trend during the period from WS6 to WS9 (Figure 5), most likely due to a decrease in  $\phi_F$  during that period (i.e., a flatter relationship between  $\phi_P$  and  $\phi_F$ ), and the limited number of light regimes in the middle of the light-response curves. The breakpoints were again observed to decline markedly after 10 days of progressive water stress. For example, the breakpoint at WS12 occurred at  $\phi_P = 0.12$  (Figure 5).

### 2.5. The Performance of the rMLR Model

The trained parameters were applied to the testing dataset, and the resulting model performance in simulating  $V_{cmax}$ ,  $J_{max}$ ,  $\phi_P$ , NPQ,  $A_{net}$ , and  $G_S$  was quantified using linear regression analysis and described using the coefficient of determination ( $R^2$ ) and the root mean squared error (RMSE) between the simulated and measured values.

A relatively small decrease was observed in both  $V_{cmax}$  and  $J_{max}$  between WS1 and WS6 (Figure 6). As the drought continued, however, they dropped substantially, and were almost zero after WS10 (Figure 6). As water stress progressed, the rMLR model was able to track the decreasing trends in  $V_{cmax}$ , and  $J_{max}$  well, explaining 83% (RMSE =  $8.25 \mu\text{mol m}^{-2} \text{s}^{-1}$ , Figure 6a) and 79% (RMSE = 24.35%, Figure 6b) in their variance between WS1 and WS12. However, the model tended to underestimate the large values of  $V_{cmax}$ , and  $J_{max}$  during WS1-WS6, and overestimate the small values between WS7 and WS9 (Figure 6).

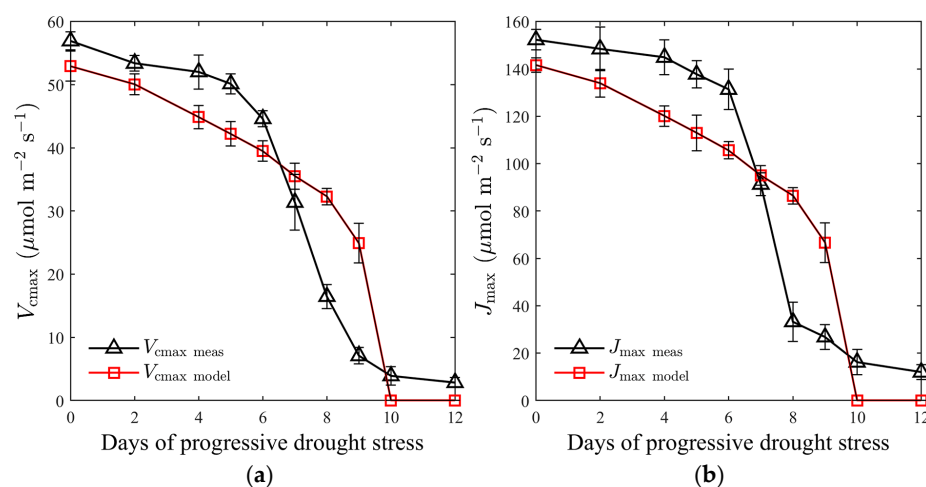


**Figure 6.** (a) Comparisons of measured versus simulated  $V_{cmax}$  ( $\mu\text{mol m}^{-2} \text{s}^{-1}$ ,  $V_{cmax \text{ meas}}$  vs.  $V_{cmax \text{ model}}$ ) between 1 and 12 days after imposing drought stress; (b) comparisons of measured versus simulated  $J_{max}$  ( $\mu\text{mol m}^{-2} \text{s}^{-1}$ ,  $J_{max \text{ meas}}$  vs.  $J_{max \text{ model}}$ ) between 1 and 12 days after imposing drought stress. Datapoints and error bars represent the mean and standard deviation of four replicates.

During the first week of the experiment,  $\phi_P$  gradually declined from 1.0 to approximately 0.3 as PAR increased from 0 to  $1000 \mu\text{mol m}^{-2} \text{s}^{-1}$  (Figure 7). As the drought intensified,  $\phi_P$  became less responsive to PAR:  $\phi_P$  decreased more steeply with increased PAR and leveled off over a broader range of light intensities (Figure 7). The simulated  $\phi_P$  light-curve shapes were similar to those estimated from the fluorescence parameters: between WS1 and WS12, the model explained 94.3% of the variation in  $\phi_P$  (RMSE = 0.07, Figure 7). Under severe water stress conditions (WS8–WS12), the model underestimated  $\phi_P$ , with  $R^2 = 0.93$  (RMSE = 0.08, Figure 7).

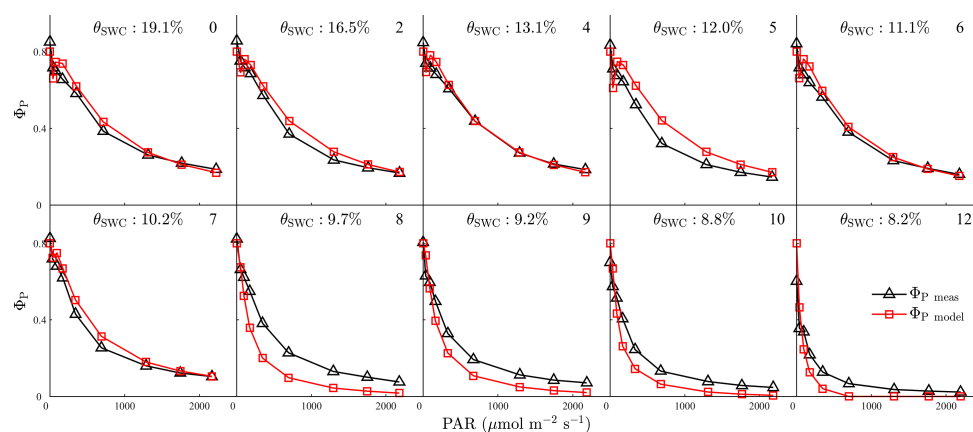


**Figure 7.** The measured versus simulated quantum yield of photochemical quenching in PSII ( $\Phi_P$ ) during light–response curves between 1 and 12 days after imposing drought stress. The soil water content ( $\theta_{SWC}$ , %) of progressive drought stress treatment is indicated. The number in the upper right corner of each plot indicates the day of progressive drought stress.

The NPQ light–response curves have an approximately opposite form to those of  $\Phi_P$ . NPQ tended to saturate at lower PAR levels with an increase in the water deficit, and substantially decrease under severe stress (Figure 8). The proposed model was able to track the light response of NPQ well:  $R^2$  between measured and modelled NPQ reached a value of 0.97 (RMSE = 0.16) for the period between WS0 and WS12 (Figure 8). The decrease in  $\theta_{SWC}$  had no obvious effect on the performance of the model in simulating NPQ, with  $R^2$  remaining at 0.97 between WS9 and WS12 (RMSE = 0.16, Figure 8). Despite the overall good performance, a small underestimation in NPQ was observed under high light intensities (PAR > 1700  $\mu\text{mol m}^{-2} \text{s}^{-1}$ , Figure 8).

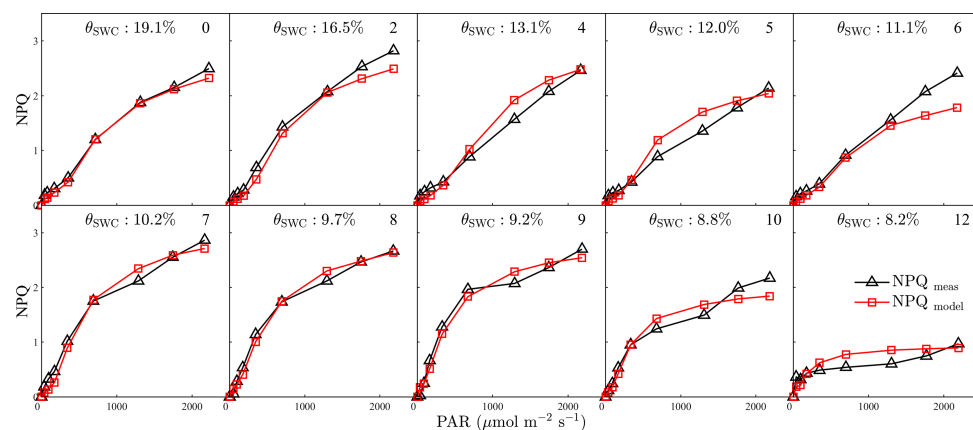


**Figure 8.** Measured versus simulated non-photochemical quenching (NPQ) during light–response curves between 1 and 12 days after imposing drought stress. The soil water content ( $\theta_{SWC}$ , %) of progressive drought stress treatment is shown. The day of progressive drought stress is indicated by the number in the upper right corner of each plot.

The simulated response of  $A_{net}$  to variations in light intensity shows a similar pattern to the response measured by the gas-exchange system: simulated  $A_{net}$  increases rapidly with increasing illumination intensity at low light levels, and gradually reaches a plateau under high light conditions (Figure 9). The rMLR model is able to reproduce  $A_{net}$  well under drought conditions; it accounted for 97.2% (RMSE = 1.532  $\mu\text{mol m}^{-2} \text{s}^{-1}$ ) of the variability in  $A_{net}$  from WS0 to WS12 (Figure 9). However, the model did tend to consistently overestimate  $A_{net}$ , with the degree of overestimation appearing to be independent of the severity of drought; simulated  $A_{net}$  was about 15% higher than measured  $A_{net}$  in

non-stressed plants and in plants subjected to mild drought (Figure 9), with the extent of overestimation varying between 10% and nearly 50% for moderate and severe drought, respectively (Figure 9). The constant value used for the  $\phi_{P_{max}}$  value (0.8) is one possible explanation for the overestimation. A decreased  $\phi_{P_{max}}$  has been suggested to occur under water stress [1,35,36]. An overestimation of  $\phi_{P_{max}}$  in drought would lead to an overestimation in  $\chi$  (Equation (12)) and then in NPQ (Equation (10)), and would consequently lead to a higher simulated  $A_{net}$  than that observed (NPQ occurs in the numerator of the rMLR model, Equation (3)).

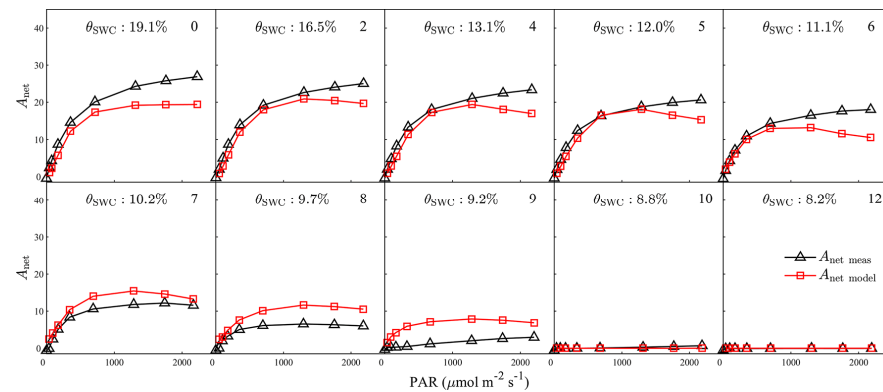


**Figure 9.** Measured versus simulated net photosynthetic carbon assimilation ( $A_{net}$ ,  $\mu\text{mol m}^{-2} \text{s}^{-1}$ ) during light–response curves between 1 and 12 days after imposing drought stress. The soil water content ( $\theta_{SWC}$ , %) of progressive drought stress treatment is indicated. The number in the upper right corner of each plot indicates the day of progressive drought stress.

Overall, the simulated  $G_s$  can explain 91.7% (RMSE =  $0.044 \mu\text{mol m}^{-2} \text{s}^{-1}$ ) of the variability in the measurements of  $G_s$  collected between WS0 and WS12 (Figure 10). The rMLR model overestimated  $G_s$  for non-stressed plants (WS0) by about 15%. However, the overestimation was suppressed from the beginning of the drought-stress period: the RMSE between simulated and measured  $G_s$  decreased to  $0.040 \mu\text{mol m}^{-2} \text{s}^{-1}$  (WS1–WS12) for the water-stressed plants (Figure 10). In particular, the proposed model demonstrated good potential for mimicking the fast drop in stomatal conductance ( $R^2 = 0.89$  and RMSE =  $0.035 \mu\text{mol m}^{-2} \text{s}^{-1}$ ) in the early stages of water stress (WS1–WS4). The overestimation of  $G_s$  at WS0 can be explained by the overestimation in  $A_{net}$  (Figure 9). The decrease in  $\beta_s$  as drought became more severe tended to cancel out the negative effect of overestimation in  $A_{net}$  (Equation (21)), resulting in an improvement in the simulation of  $G_s$ .

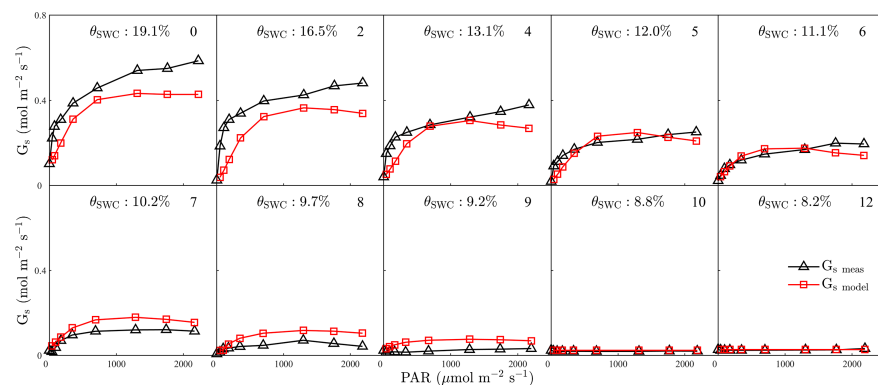


**Figure 10.** Measured versus simulated stomatal conductance ( $G_s$ ,  $\text{mol m}^{-2} \text{s}^{-1}$ ) during light–response curves between 1 and 12 days after imposing drought stress. The soil water content ( $\theta_{SWC}$ , %) of progressive drought stress treatment is shown. The day of progressive drought stress is indicated by the number in the upper right corner of each plot.

### 3. Discussion

Identification of the cascade of drought-induced changes in photosynthetic characteristics is highly relevant to fully understanding the relationships between photosynthesis, NPQ, and fluorescence under water stress conditions. Stomatal closure is the earliest response to drought, paralleling a decrease in photosynthetic CO<sub>2</sub> assimilation but with a lower magnitude (Figure 2). In the early stages of drought stress, exposure to the volatile plant hormone methyl jasmonate (MeJA) can mitigate drought stress by stomatal closure [37–39]. During WS1–WS6, under mild-to-moderate water stress, energy partitioning in PSII (i.e.,  $\phi_P$ ,  $\phi_N$ ,  $\phi_D$ , and  $\phi_F$ ) remained virtually unchanged under low or intermediate light levels (Figure 4). However, we noticed a decline in  $\phi_P$ , and a rise in the other three pathways,  $\phi_D$ ,  $\phi_N$  and  $\phi_F$ , in the presence of high light levels during that period (Figure 4). These observations may suggest that the proportion of energy dissipated in each pathway does not change much regardless of stomatal closure levels during the initial period of drought [40].

At moderate-to-severe drought (WS7–WS9),  $G_S$  almost vanished (Figure 2) and the observed drop in  $A_{net}$  indicated the predominance of non-stomatal limitations to photosynthesis [41]. Given the lower  $G_S$ , the excess light energy can ultimately lead to the production of reactive oxygen species and reflect the MeJA response [37–39]. As a consequence,  $\phi_P$ , the quantum yield of photochemistry in PSII, showed a decreasing trend, especially at high light levels (Figure 4). To compensate for the decline in  $\phi_P$ , regulated heat dissipation ( $\phi_N$ ) tended to increase as a main photoprotective mechanism, and  $\phi_D$  remained fairly constant (Figure 4). The engagement of thermal energy dissipation also resulted in a small decrease in  $\phi_F$ .

Under extreme drought conditions (WS10–WS12),  $\phi_P$  continued to decrease, and the stressed plants kept increasing their use of thermal energy dissipation and fluorescence emission ( $\phi_F$ ) to cope with excess light energy (Figure 4). However, the process of thermal energy dissipation changed from a regulated form that can be rapidly activated by excess light to a sustained form that is rather insensitive to fluctuating light [42,43], resulting in the simultaneous rise of  $\phi_D$  and decline of  $\phi_N$  (Figure 4). This result is consistent with the findings that this transformation of energy dissipation characteristics tends to occur during periods of harsh environmental stress [44].

The results confirm that water stress increases nonlinearity in the overall relationship between photosynthesis and fluorescence (Figure 3). Under typical high light levels, as what might occur for early afternoon spaceborne SIF retrievals, the ‘NPQ phase’, driving a positive SIF-GPP relationship, is representative of non-stressed plants. We showed that the transition from the ‘PQ phase’ to the ‘NPQ phase’ is driven by both irradiance and the severity of drought. During moderate or severe drought stress, the decrease in  $\phi_P$ , and increase in  $\phi_F$ , pushes the stressed plant from the ‘NPQ phase’ to the ‘PQ phase’, resulting in a more nonlinear SIF-GPP relationship when considering both the drought and non-drought periods together.

When the stomata are closed, Marrs et al. (2020) [16] found that the photosynthetic rate decreases rapidly, and SIF is relatively less affected. SIF cannot track the changes of photosynthesis, resulting in the phenomenon of decoupling fluorescence and photosynthesis. During a short drought duration, Helm et al. (2020) [29] showed that the degree of reduction in leaf photosynthesis was much greater than the reduction in SIF. These studies are consistent with our findings. Our results also show that the fluorescence response to water stress occurs later, and at a smaller magnitude, which appears to contradict studies using satellite SIF, suggesting a strong negative response [26,27]. Such a dichotomy can be resolved by assessing the relative importance of the structural and physiological contributions to the drought response of fluorescence at different scales. Fluorescence variations reported in leaf-scale studies are driven by changing fluorescence efficiencies alone (unless absorbed PAR is unchanged) which, as shown here, has a relatively muted sensitivity to water stress. However, at the whole-plant or canopy scales, both structural and physiologic components may regulate TOC SIF, and so a drought-induced decline in absorbed PAR due

to canopy structural changes (i.e., changes in leaf area or leaf angles) dominates negative anomalies observed in satellite SIF [27,45]. It is worth noting that these seemingly inconsistent results should not necessarily be viewed as a failure of SIF for monitoring plant water stress, as the changes in canopy structure may also directly reflect the plant water status. The inconsistency also highlights the need to consider/normalize canopy structure factors during drought. Otherwise, we may run the risk of wrongly assigning physiological causality to variance in TOC SIF due to changes in the canopy structure [28].

Equation (3) also contains other parameters (for example,  $K_{DF}$ ,  $K_{mc}$ ,  $K_{mc}$ ,  $\Gamma^*$  and  $\Phi_{Pmax}$ ). These additional parameters are often assumed to be constant in the literature but may actually vary with water stress. The actual  $K_{DF}$  value is currently unknown. Gu et al. (2019) [31] set  $K_{DF}$  to 19, while Liu et al. (2022) [46] assumed  $K_{DF}$  to be 9. According to Equation (3), using these two  $K_{DF}$  values will directly cause  $A_{net}$  to change by a factor of two.  $K_{DF}$  remains unchanged at the same temperature, but there is currently no relevant research on  $K_{DF}$  under water stress.  $K_{mc}$ ,  $K_{mc}$  and  $\Gamma^*$  depend on the partial pressure of oxygen and temperature, which are related to the specificity factor of Rubisco [47]. Furthermore,  $\Phi_{Pmax}$  decreases under water stress conditions. Considering these potential effects of water stress on the parameters involved in our theoretical equations, more future measurements are needed to quantitatively examine their relationships under water conditions. We performed a sensitivity analysis on the MLR model. The input variables are  $C_i$ ,  $K_{co}$ ,  $\Gamma^*$ ,  $\Phi_{Pmax}$ ,  $q_L$ , and  $ChlF_{P-F}$ , respectively. The sensitivity analysis results show that the main parameters affecting  $A_{net}$  variation are leaf physiological parameters,  $q_L$  and  $ChlF_{P-F}$ . These two parameters explain more than 80% of the  $A_{net}$  variation, while other leaf physiological parameters with greater influence such as  $C_i$ ,  $K_{co}$ , and  $\Phi_{Pmax}$  account for more than 15% of the total variation. However, the parameter  $\Gamma^*$  plays a small role in explaining the  $A_{net}$  variation. Han et al. (2022) [47] studied the relationship between SIF and GPP through the MLR model and showed that the  $q_L$  is sensitive to light intensity and can be expressed by the exponential equation of two parameters ( $aq_L$  and  $bq_L$ ) between the  $q_L$  and PAR. However, we found that in the uniform plant functional types, the parameters  $aq_L$  and  $bq_L$  vary greatly. Therefore, we use the NPQ/ $\Phi_P$  version of the  $J_a$ - $ChlF_{P-F}$  equation. The NPQ/ $\Phi_P$  version mixes photochemistry and non-photochemistry. Further, this mixing is superficial because information on non-photochemistry is canceled out in the product of  $(1 + NPQ)$  and  $\Phi_P/(1 - \Phi_P)$  as  $\Phi_P$  contains both photochemical and non-photochemical information. We need to consider both the energy-dependent and energy-independent components of NPQ. This is particularly important for this study because it focuses on water stress, which likely induces energy-independent NPQ.

The weak response of fluorescence to a water deficit suggests that SIF alone, at least its physiological component, is not able to track drought-induced changes in plant physiology. However, the development of the rMLR model allows for a mechanistic understanding of the drought impact on photosynthetic characteristics using SIF, soil moisture, and two measurable meteorological variables as the inputs. To apply the rMLR model at the canopy scale, that is, by using narrowband SIF<sub>toc</sub> as an input variable for Equation (3), several more steps will need to be performed. First, the contribution of PSII fluorescence to SIF<sub>toc</sub> ( $f_{PSII}$ ) should be determined. Although Bacour et al. [48] showed that  $f_{PSII}$  can be also estimated from  $T_{air}$  and PAR, more research is needed to assess how  $f_{PSII}$  varies with species and environmental conditions [44]. Second, the probability of a fluorescence photon escaping from a leaf level to canopy scale ( $f_{esc\_L-C}$ ) must be quantified, in addition to  $f_{esc\_P-L}$  (Equation (8)). In the near-infrared (NIR) region,  $f_{esc\_L-C}$  can be estimated from directional reflectance (RNIR) [49]. Note that both SIF<sub>toc</sub> and RNIR can be concurrently obtained from measurements of irradiance/radiance [50]. Thus, the estimation of  $f_{esc\_L-C}$  requires no additional observations. Third, a full-band SIF emission should be reconstructed from narrowband SIF. The full SIF spectrum at TOC can be approximated by a linear combination of basis spectra [46,51,52]. The Soil-Canopy Observations of Photosynthesis and Energy Balance (SCOPE) [53] model is typically used to generate a dataset that is representative of the majority of actual scenes. Principal Component Analysis (PCA) or

Singular Value Decomposition (SVD) techniques are then applied to extract the basis spectra from this simulated dataset. However, the SCOPE model is designed for homogeneous vegetation canopies, such as crops, and its performance may deteriorate for a heterogeneous, structurally complex canopy [54]. Finally, a large-scale, and near-real-time root-zone soil moisture (RZSM) dataset is needed to estimate  $\beta_S$  and  $\beta_B$ . Since satellite soil moisture satellite observations are sensitive to surface soil moisture, typically within the first few centimeters, current RZSM datasets are mostly produced by assimilating observations into model simulations [55,56].

## 4. Materials and Methods

### 4.1. Leaf-Scale Concurrent Instrumentation

We developed a leaf-scale concurrent measurement system by integrating a portable gas-exchange system (LI-COR Biosciences, Lincoln, NE, USA), two HR2000+ spectrometers and two QE Pro spectrometers (Ocean Optics, Dunedin, FL, USA), a PAM system (Dual-PAM-100, Heinz Walz GmbH, Effeltrich, Germany), a short-pass filter, an external LED light source and fiber optics (connecting the PAM and spectrometers to the leaf chamber) (Figure 11). With this measurement system, we were able to simultaneously measure gas-exchange, passive and active ChlF, reflectance and transmittance for plants under a variety of controlled environmental conditions [46,57]. The main components and modifications are discussed below.

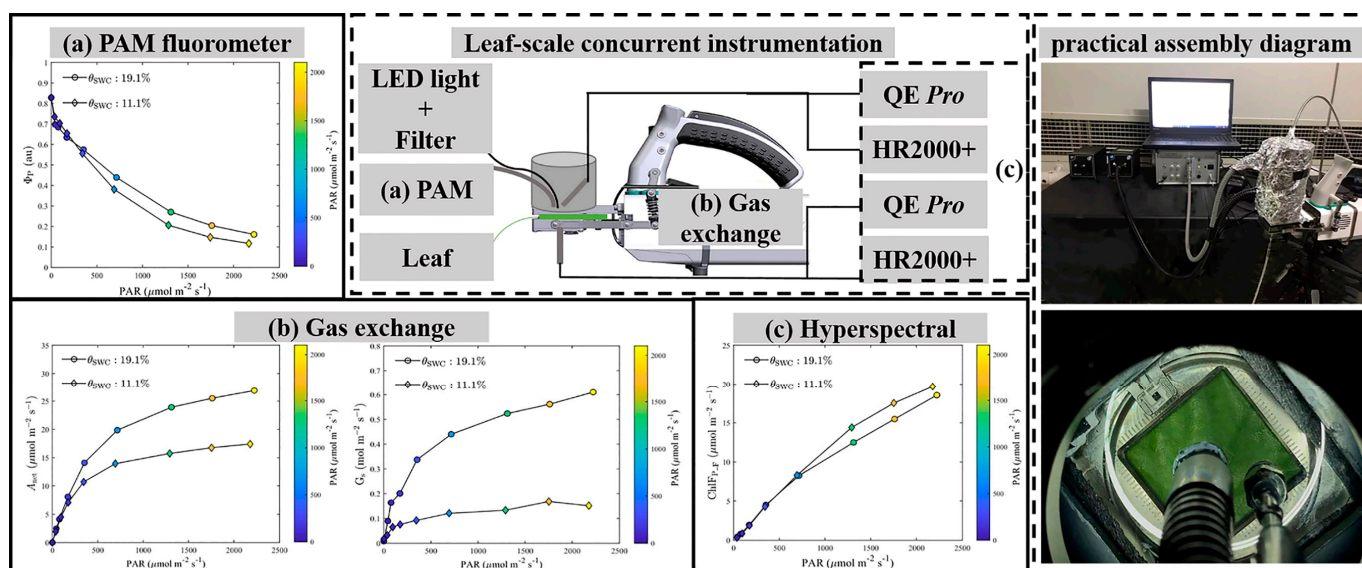


**Figure 11.** Schematic of the leaf-scale concurrent light–response curve measurement system. The following measurements were taken: (a) pulse amplitude modulation (PAM) fluorometer (the quantum yields of photochemical quenching in photosystem II ( $\phi_P$ ) and photochemically active radiation (PAR) are shown). (b) Gas exchange (net CO<sub>2</sub> assimilation rate in light–response curves). (c) Chlorophyll fluorescence flux density emitted from photosystem II ( $\text{ChlF}_{P-F}$ ,  $\mu\text{mol m}^{-2} \text{s}^{-1}$ ), retrieved from the full ChlF emission spectrum. The external light source was attenuated by a customized 625 nm short-pass filter (not shown). A practical photograph of the leaf-scale concurrent measurement system which includes an LI-6800 gas-exchange chamber, a Dual-PAM-100 fluorometer, two HR2000+ spectrometers and two QE Pro spectrometers.

#### 4.1.1. Gas-Exchange System

We used the LI-6800 gas-exchange system to control the environmental conditions of a modified leaf chamber. The original film of the LI-6800 transparent leaf chamber was replaced with high-transparency plexiglass. An external LED light source (see below) was fixed to the high-transparency plexiglass via a cylindrical plastic tube. The optical fibers of the PAM fluorometer and spectrometer were inserted into the leaf chamber via two fiber

adapter bulkheads added to the plastic tube. These optical fibers were fixed to the diagonal of the fiber adapter bulkhead. In order to measure downward chlorophyll fluorescence spectral radiant energy fluxes, a metal plate covering the base of the leaf chamber was first added, and a fiber adapter bulkhead for inserting optical fibers was then fixed in the middle of this plate. All the fiber adapter bulkheads were sealed with clay to ensure the leaf chamber remained air-tight. To reduce light scattering in the leaf chamber, the inside of the light-source plastic tube and the upper surface of the metal plate connected to the base of the leaf chamber were painted with black acrylic paint (Black 2.0, Stuart Semple, UK) as a light trap (Figure 11b). The modified gas-exchange system blocks all light, except for incoming light with wavelengths longer than 625 nm, using a short-pass filter.

#### 4.1.2. Gas-Exchange System

A Dual-PAM-100 instrument (Heinz Walz GmbH, Effeltrich, Germany) was used to measure fluorescence parameters. The Dual-PAM-100 featured a single red (625 nm) power LED for excitation of chlorophyll fluorescence. The saturating pulse was also driven by the red LED, which emitted a consistent  $10,000 \mu\text{mol m}^{-2} \text{s}^{-1}$  for 0.8 s. The Dual-PAM-100 induced the maximum fluorescence quantum yield using the saturation pulse under dark-adapted conditions. The PAM was connected to the leaf chamber via a 1 m long single fiber of 0.8 cm diameter routed through the entrance hole (Figure 11a). The angle between the PAM fiber tip inserted into the entrance hole and the plane of the leaf chamber was kept at about  $90^\circ$  and the vertical distance between the fiber optic head and the surface of the leaf sample was maintained at 1 cm to avoid blocking the field of view of the PAM instrument.

#### 4.1.3. Spectrometers

Using two HR2000+ and two QE *Pro* (Ocean Optics, Dunedin, FL, USA) high-sensitivity spectrometers, we simultaneously measured reflection, transmission, and upward and downward chlorophyll fluorescence spectral radiant energy fluxes of the leaf (Figure 11c). The leaf chamber was linked to the four spectrometers by means of two bifurcated optical fibers. One of these fibers was inserted into the top fiber adapter bulkhead above the leaf chamber to connect to an HR and a QE *Pro*, while the other was inserted into the bottom of the leaf chamber and connected to the other HR and QE *Pro*. Both bifurcated fibers had a diameter of 1000  $\mu\text{m}$  to ensure they could collect enough light. The vertical distance between the tip of the top fiber and the sample surface of the leaf was kept at 10 mm to allow for measurement of the upward chlorophyll fluorescence. The lower fiber optic head was inserted vertically into the base of the leaf chamber to measure the downward chlorophyll fluorescence, with the distance from the back of the leaf being 10 mm. The HR2000+ spectrometers covered the 296–1203 nm range at an optical resolution of 5.3159 nm with a spectral sampling of 0.4430 nm. The detector of the QE *Pro* spectrometer covered the range 634–863 nm at an optical resolution of 5.2656 nm with a spectral sampling of 0.2194 nm. The absolute calibration of the spectrometers and all light paths were carried out by using a separate reference QE *Pro* spectrometer (Ocean Optics, Dunedin, FL, USA) calibrated using a NIST traceable integration sphere. Dark current and non-linear spectrometer calibrations were completed before each measurement.

#### 4.1.4. Light Source

The external actinic light source was a white LED light source (S5000, Nanjing Hecho Technology Co., Nanjing, China) with a ring-shaped fiber which provided a homogeneous light distribution across the leaf chamber. The actinic light source was capable of delivering  $0\text{--}3000 \mu\text{mol m}^{-2} \text{s}^{-1}$  with a 400–700 nm wavelength range. To attenuate this LED light source, a customized 625 nm short-pass, fused silica filter with a diameter of 12.5 mm was placed between it and the O-ring fiber optic (Figure 11). After short-pass filtering, the rejection wavelength range of the external light source was, in fact, 639–925 nm, due to insufficient accuracy. In the 350–612 nm range, the transmittance exceeded 91% and the optical density was 4 (Edmunds Optics, Barrington, NJ, USA). A tin-foil lampshade outside

the cylindrical plastic tube was used to block outside light. The light intensity was varied in the range of 0–2500  $\mu\text{mol m}^{-2} \text{s}^{-1}$  by adjusting the pulse-width modulation controller in the light source.

#### 4.2. Experiment Design

The experiment was conducted between 15 October 2020 and 30 April 2021 in the Northwest A&F University, Yangling, China. Winter wheat (*Triticum aestivum* L. cultivar Xi Nong 979) was sown in plastic pots (27 cm height  $\times$  21 cm diameter) filled with 9 kg of sieved, air-dried, loess topsoil and 1.95 g of urea. The field capacity of the soil was 24% and the wilting point was 9%. The plants were grown under a rainproof shed until the turning-green stage, and then moved to a climate chamber where  $\text{CO}_2$  concentration, air temperature and relative humidity were controlled at 400  $\mu\text{mol mol}^{-1}$ , 12 °C and 60%. The light intensity above the canopy during the experiment was kept at 600  $\mu\text{mol m}^{-2} \text{s}^{-1}$  for 12 h per day, from 8 a.m. to 8 p.m. Beginning in late March, eight representative wheat plants in the heading stage were chosen for the experiment.

Throughout the 28-day experiment, the gravimetric soil water content ( $\theta_{\text{SWC}}$ , %) was continuously monitored using the weighing method [58,59]. The wheat plants were subjected to one of two treatments: non-water stress (NS) and water stress (WS). Four wheat plants in each treatment were randomly selected as biological replicates. In the NS treatment, the  $\theta_{\text{SWC}}$  was maintained at 19.1% (well-watered plants, assuming 80% of field capacity) [60,61] throughout the experiment, but, in the WS treatment, to simulate intensifying drought,  $\theta_{\text{SWC}}$  was gradually decreased to a final value of 6.3%. This steady decline in  $\theta_{\text{SWC}}$  ensured that plants under the WS treatment were subjected to progressive drought stress [62].

Measurements were made on attached leaves of the wheat plants under the two water treatments. The wheat leaf had to be placed in the 3 cm  $\times$  3 cm clear chamber along the diagonal of the square and positioned in the chamber with its adaxial surface facing the LED light source. Since the leaves did not fill the leaf chamber, the area of each leaf had to be accurately measured. After 1 h of dark adaptation, a saturation flash from the PAM fluorometer was used to determine minimal fluorescence ( $F_0$ ) and maximal fluorescence in the dark ( $F_m$ ) of dark-adapted leaves. Next, the light–response curves and  $\text{CO}_2$  response curves of gas exchange and fluorescence were measured. The  $\text{CO}_2$  flow rate, air relative humidity and leaf temperature were kept constant at 500  $\mu\text{mol s}^{-1}$ , 50% and 12 °C, respectively. To obtain light–response curves, measurements were conducted at a  $\text{CO}_2$  concentration of 400  $\mu\text{mol mol}^{-1}$ . Light–response measurements were made with photochemically active radiation (PAR) light intensities of 0, 40, 90, 180, 350, 700, 1300, 1700, and 2100  $\mu\text{mol m}^{-2} \text{s}^{-1}$ . Next, we measured the  $\text{CO}_2$  response curve under saturated light intensity (1500  $\mu\text{mol m}^{-2} \text{s}^{-1}$ ) using values of the  $\text{CO}_2$  concentration gradient of 30, 50, 100, 200, 300, 400, 600, 900, 1200, 1500  $\mu\text{mol mol}^{-1}$ .

Throughout the course of each light–response curve and  $\text{CO}_2$  response curve determination, spectral measurements (reflected radiance, transmitted radiance, forward and backward fluorescence spectral radiant energy flux) were continually recorded at 1 s intervals. Steady-state fluorescence emission ( $F_t$ ), induced by the measuring beam of the PAM fluorometer, was also included. Maximal fluorescence emission in the light-adapted state ( $F_m'$ ) from the PAM was recorded under each light intensity and  $\text{CO}_2$  concentration. From these measurements ( $F_0$ ,  $F_t$ ,  $F_m$ ,  $F_m'$ ), we also obtained NPQ, a fraction of open PSII reaction centers ( $q_L$ ) [63], and the actual rate of electron transport ( $J_{a\text{-PAM}}$ ,  $\mu\text{mol m}^{-2} \text{s}^{-1}$ ). The details for estimating them are provided in Note S1. Net  $\text{CO}_2$  assimilation rate ( $A_{\text{net}}$ ,  $\mu\text{mol m}^{-2} \text{s}^{-1}$ ) and stomatal conductance to water vapor ( $G_s$ ,  $\text{mol m}^{-2} \text{s}^{-1}$ ) provided by the gas-exchange system were automatically stored every 5 s. To ensure that the gas-exchange conditions were stable, the measurements for light curves and  $\text{CO}_2$  curves were made after waiting at least 5 min, and up to 20 min, between each light intensity or  $\text{CO}_2$  concentration change. The filtered incident radiation of the LED light source at each light intensity were measured with a standard reflectance panel (Spectralon; Labsphere, North

Sutton, NH, USA). The above measurements were taken at day 0 (before the water stress treatment started, WS0) and at days 2, 4, 5, 6, 7, 8, 9, 10, 12, 14, 16, 18, 20, 22, 24, 26, 28 after withholding water (WS2, WS4, etc., respectively). At WS0, the unstressed maximum carboxylation capacity of Rubisco ( $V_{\text{cmax},0}$ ,  $\mu\text{mol m}^{-2} \text{s}^{-1}$ ) and the unstressed maximum electron transport rate ( $J_{\text{max},0}$ ,  $\mu\text{mol m}^{-2} \text{s}^{-1}$ ) were estimated by fitting the FvCB model [64] to the  $\text{CO}_2$  response curves. According to the photosynthetic light–response curve of winter wheat at WS0,  $A_{\text{net}}$  increased steeply with PAR when  $\text{PAR} \leq 350 \mu\text{mol m}^{-2} \text{s}^{-1}$ , and increased slowly with increasing PAR when  $\text{PAR} \geq 1000 \mu\text{mol m}^{-2} \text{s}^{-1}$  (see below). Thus, a PAR level between 350 and  $1000 \mu\text{mol m}^{-2} \text{s}^{-1}$  was assumed to be the intermediate light condition, and PAR levels lower than 350 or higher than  $1000 \mu\text{mol m}^{-2} \text{s}^{-1}$  were taken to be low and high light conditions, respectively.

#### 4.3. The Reformulated MLR (rMLR) Model

The MLR model [31] shows that  $J_a$  can be mechanistically estimated from  $q_L$ ,  $\Phi_{\text{Pmax}}$ , and the chlorophyll fluorescence flux density emitted from the photosystem II (PSII) across the full ChlF emission spectrum ( $\text{ChlF}_{\text{P-F}}$ ,  $\mu\text{mol m}^{-2} \text{s}^{-1}$ ). At the photosystem level,

$$J_a = \frac{q_L \times \Phi_{\text{Pmax}} \times (1 + K_{\text{DF}}) \times \text{ChlF}_{\text{P-F}}}{(1 - \Phi_{\text{Pmax}})}, \quad (1)$$

where  $K_{\text{DF}}$  is the ratio between the rate constants for constitutive heat loss ( $K_{\text{D}}$ ) and fluorescence ( $K_{\text{F}}$ ) and is assumed to be 9 [46]. However,  $q_L$  is much less studied than the other PAM parameters [31]. A previous study [46] shows that the role of  $q_L$  and  $\Phi_{\text{Pmax}}$  in the original MLR model can be replaced by  $\Phi_{\text{P}}$  and NPQ:

$$J_a = \frac{\Phi_{\text{P}} \times (1 + \text{NPQ}) \times (1 + K_{\text{DF}}) \times \text{ChlF}_{\text{P-F}}}{(1 - \Phi_{\text{P}})}, \quad (2)$$

The practical advantage of Equation (2) is that both  $\Phi_{\text{P}}$  and NPQ (dimensionless) can be estimated from air temperature ( $T_{\text{air}}$ ,  $^{\circ}\text{C}$ ) and PAR (see the section on the estimation of  $\Phi_{\text{P}}$  and NPQ). Note that  $J_a$  in Equations (1) and (2) is already balanced by carboxylation and photorespiration [31,47]. To differentiate from  $J_{a\_PAM}$ , in this study,  $J_a$  was calculated from ChlF emission using Equation (2).

One can obtain  $A_{\text{net}}$  for  $\text{C}_3$  and  $\text{C}_4$  species:

$$A_{\text{net}} = A_{\text{g}} - R_{\text{d}} = \begin{cases} \frac{C_c - \Gamma^*}{4C_c + 8\Gamma^*} \times \frac{\Phi_{\text{P}} \times (1 + \text{NPQ}) \times (1 + K_{\text{DF}}) \times \text{ChlF}_{\text{P-F}}}{(1 - \Phi_{\text{P}})} - R_{\text{d}} & \text{C}_3 \\ \frac{1 - \zeta}{3} \times \frac{\Phi_{\text{P}} \times (1 + \text{NPQ}) \times (1 + K_{\text{DF}}) \times \text{ChlF}_{\text{P-F}}}{(1 - \Phi_{\text{P}})} - R_{\text{d}} & \text{C}_4 \end{cases}, \quad (3)$$

where  $A_{\text{g}}$  represents gross photosynthesis ( $\mu\text{mol m}^{-2} \text{s}^{-1}$ );  $R_{\text{d}}$  is the daytime respiration ( $\mu\text{mol m}^{-2} \text{s}^{-1}$ );  $C_c$  is the chloroplastic  $\text{CO}_2$  partial pressure ( $\mu\text{mol mol}^{-1}$ );  $\Gamma^*$  is the chloroplastic compensation point of  $\text{CO}_2$   $\mu\text{mol mol}^{-1}$  [31,65];  $\zeta$  is the fraction of total electron transport of mesophyll and bundle sheath allocated to mesophyll, assumed to be 0.4 [66]. We refer to Equation (3) as the rMLR model. The procedure for quantifying  $A_{\text{net}}$  from the observed SIF is illustrated in Figure 12.

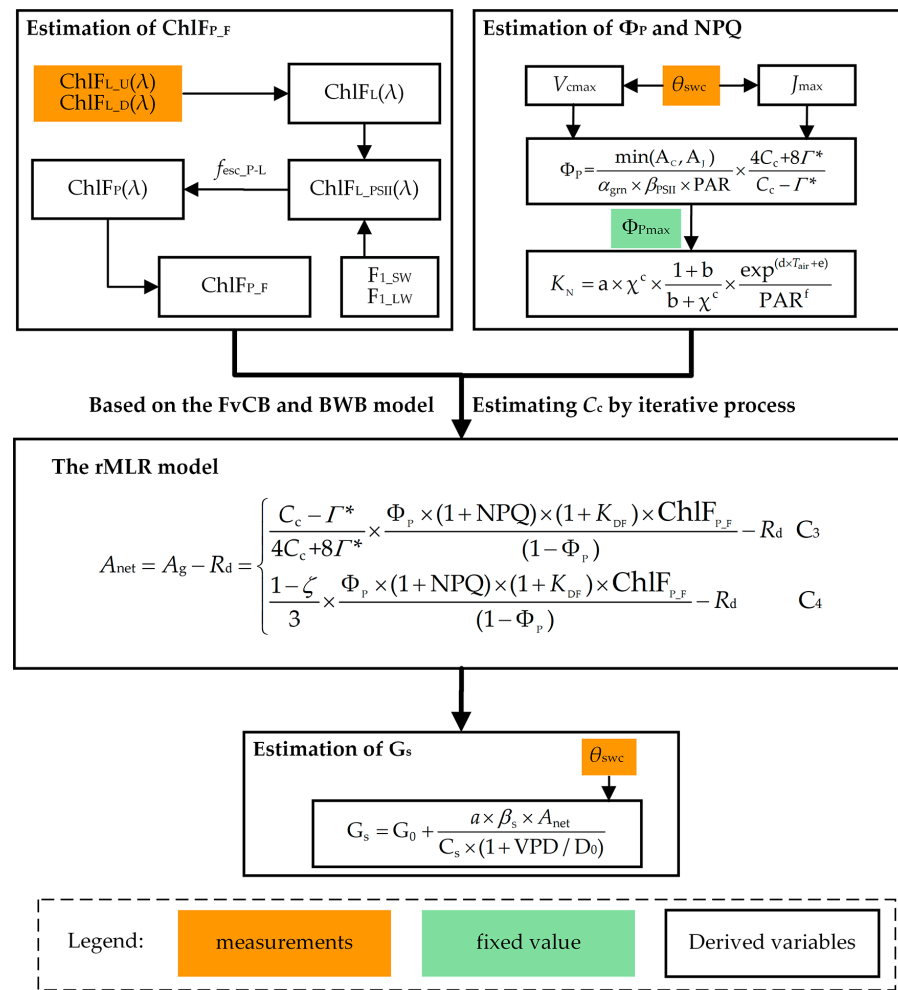


**Figure 12.** Flowchart for quantifying the net  $\text{CO}_2$  assimilation rate  $A_{net}$  ( $\mu\text{mol m}^{-2} \text{s}^{-1}$ ) from the passive ChlF spectrum. The definitions of the variables are listed in Appendix A.

#### 4.4. Correction for the PSI Fluorescence

The rMLR model is only valid for fluorescence emissions from PSII [31]; the contribution of the PSI fluorescence should be excluded from all actively and passively induced ChlF related to Equation (3). Using the far-red method, Pfündel et al. [67] showed that the PSI fluorescence yield ( $F_1$ ) detected by the PAM fluorometer for  $C_3$  species can be estimated as:

$$F_1 = 0.24 \times F_o, \quad (4)$$

By subtracting  $F_1$  from the fluorescence yields ( $F_o$ ,  $F_m$ ,  $F_m'$ ,  $F_t$ ) directly measured by the PAM fluorometer, we were able to correct them for PSI fluorescence. Accordingly, all other yields/parameters derived from these four yields,  $\Phi_P$ ,  $\Phi_F$ ,  $\Phi_N$ ,  $\Phi_D$ , and NPQ, were also corrected for PSI fluorescence. See the details in Note S1. Hereafter, all of the active fluorescence parameters in this study only contain the PSII contribution unless otherwise specified.

The leaf-scale concurrent measurement system (Figure 11) provides the passive ChlF spectrum in the range 640 to 850 nm at the leaf scale ( $\text{ChlF}_L(\lambda)$ ,  $\text{mW m}^{-2} \text{nm}^{-1} \text{sr}^{-1}$ ):

$$\text{ChlF}_L(\lambda) = \text{ChlF}_{L-U}(\lambda) + \text{ChlF}_{L-D}(\lambda), \quad (5)$$

where  $\text{ChlF}_{L-U}(\lambda)$  and  $\text{ChlF}_{L-D}(\lambda)$  represent the fluorescence radiance emitted from adaxial and abaxial leaf surfaces ( $\mu\text{W cm}^{-2} \text{nm}^{-1} \text{sr}^{-1}$ ), respectively, and  $\lambda$  is the wavelength (nm).

Due to the strong linear relationships between spectral fluorescence yields and the original PAM  $F_t$  yields [68,69], deriving the ratio of  $F_t$  yields before and after correction for PSI fluorescence can also allow for an approximate separation of the PSI and PSII spectral fluorescence yields. Further, Pfündel [70] showed that the ratio of  $F_1$  to  $F_0$  was 14% and 45% in the spectral ranges below 700 nm (SW) and above 700 nm (LW), respectively. Considering the wavelength-dependent relationships among spectral and PAM fluorescence yields [69], the contribution of PSII ( $\text{ChlF}_{L\_PSII}(\lambda)$ ) to measurements of  $\text{ChlF}_L(\lambda)$  can be estimated as:

$$\text{ChlF}_{L\_PSII}(\lambda) = \begin{cases} \text{ChlF}_L(\lambda) \times \frac{F_t - F_{1\_SW}}{F_t} & \lambda \leq 700 \text{ nm} \\ \text{ChlF}_L(\lambda) \times \frac{F_t - F_{1\_LW}}{F_t} & \lambda > 700 \text{ nm} \end{cases}, \quad (6)$$

where  $F_t$  is the steady-state fluorescence yield, and  $F_{1\_SW}$  ( $F_{1\_SW} = 0.14 \times F_0$ ) and  $F_{1\_LW}$  ( $F_{1\_LW} = 0.45 \times F_0$ ) represent the PSI contribution at SW wavelengths and LW wavelengths, respectively. Note that  $F_t$  and  $F_0$  used in Equation (6) were directly measured by the PAM fluorometer and thus contain contributions from both PSI and PSII.

To apply the rMLR model,  $\text{ChlF}_{L\_PSII}(\lambda)$  must be further downscaled to the photosystem level ( $\text{ChlF}_P(\lambda)$ ) by accounting for the probability that a fluorescence photon escapes from the PSII light reactions inside the leaves to the surface of the leaf ( $f_{\text{esc\_P-L}}$ ):

$$\text{ChlF}_P(\lambda) = (\text{ChlF}_{L\_PSII}(\lambda)) / f_{\text{esc\_P-L}}(\lambda), \quad (7)$$

$f_{\text{esc\_P-L}}$  is approximately equal to the sum of leaf reflectance ( $R$ ) and transmittance ( $T$ ) [71]:

$$f_{\text{esc\_P-L}} \approx R(\lambda) + T(\lambda), \quad (8)$$

Note that  $\text{ChlF}_P(\lambda)$  in Equation (7) has units of  $\text{mW m}^{-2} \text{nm}^{-1} \text{sr}^{-1}$ . To obtain  $\text{ChlF}_{P\_F}$  as required by Equation (3), we need to integrate  $\text{ChlF}_P(\lambda)$  between 640 and 850 nm and perform a unit conversion:

$$\text{ChlF}_{P\_F} = \sum_{\lambda=640}^{850} [\text{ChlF}_P(\lambda)] \times \frac{\lambda \times 10^6}{h \times c \times N_A \times 10^3 \times 10^9}, \quad (9)$$

where  $h$  is the Planck constant ( $6.62607015 \times 10^{-34} \text{ J}\cdot\text{s}$ ),  $c$  is the light speed ( $3 \times 10^8 \text{ m s}^{-1}$ ),  $N_A$  is the Avogadro constant ( $6.02 \times 10^{23} \text{ mol}^{-1}$ ),  $10^6$  is used to convert moles (mol) to micromoles ( $\mu\text{mol}$ ) in  $N_A$ ,  $10^3$  is used to convert milliwatts (mW) to Watts (W), and  $10^9$  is used to convert nanometers (nm) to meters (m) in  $\lambda$ . For the application of the rMLR model at the canopy scale or beyond, see the Section 3.

#### 4.5. Estimation of $\phi_P$ and NPQ

In this study,  $K_D$  and  $K_F$  are assumed to be 0.9 and 0.1, respectively [46]. Note that NPQ should be equal to the rate coefficients of energy-dependent heat dissipation ( $K_N$ ) because  $\text{NPQ} = K_N / (K_F + K_D)$ , and  $K_F + K_D = 1$ .  $K_N$  can be estimated as [48]:

$$K_N = a \times \chi^c \times \frac{1 + b}{b + \chi^c} \times \frac{\exp^{(d \times T_{\text{air}} + e)}}{\text{PAR}^f}, \quad (10)$$

where  $a$ ,  $b$ ,  $c$ ,  $d$ ,  $e$  and  $f$  are fitting parameters. Following Bacour, Maignan, MacBean, Porcar-Castell, Flexas, Frankenberg, Peylin, Chevallier, Vuichard and Bastrikov [48],  $b$ ,  $c$ ,  $d$ ,  $e$  and  $f$  are assumed to have values of 5.74, 2.167,  $-0.014$ ,  $-0.00437$  and 0.00576, respectively. Potentially, we can use an exponential equation with three parameters to represent the relationship between the parameter  $a$  and  $\theta_{\text{SWC}}$ :

$$a = g \times \exp^{((-h) \times \theta_{\text{swc}})} + j, \quad (11)$$

where  $g$ ,  $h$ , and  $j$  are empirical parameters. The measurements are randomly divided into two groups, with 50% of the data used for training, and the remaining 50% for evaluating the performance of the predictions. The Matlab function 'lsqnonlin' was used to obtain the values of the parameters by minimizing a cost function on the training dataset:  $C = (M - S)^2$ , where  $M$  is the NPQ measured with the PAM, and  $S$  is the modelled NPQ. A Trust Region algorithm was used to update the values of the parameters after each iteration step, with the iteration terminating when the improvement in the cost function was less than  $10^{-3}$ . Table S1 presents the initial values, boundaries and constraints of the parameters.

$\chi$  is defined as [32,46]:

$$\chi = 1 - \frac{\Phi_P}{\Phi_{P_{\max}}}, \quad (12)$$

where  $\Phi_{P_{\max}}$  is assumed to be 0.8 and is similar among healthy plants;  $\Phi_P$  is estimated as [32]:

$$\Phi_P = \frac{\min(A_C, A_J)}{\alpha_{\text{grn}} \times \beta_{\text{PSII}} \times \text{PAR}} \times \frac{4C_c + 8\Gamma^*}{C_c - \Gamma^*}, \quad (13)$$

where  $A_C$  and  $A_J$  represent Rubisco-limited and RuBP-limited gross  $\text{CO}_2$  assimilations ( $\mu\text{mol m}^{-2} \text{s}^{-1}$ ), respectively.  $\alpha_{\text{grn}}$  represents the absorption efficiency of PAR by green leaves, and the value is usually fixed at 0.84.  $\beta_{\text{PSII}}$  is the fraction of absorbed energy allocated to PSII, and the value is set to 0.5 [72].  $A_C$  and  $A_J$  are given by [73]:

$$A_C = \frac{V_{\text{cmax}} \times (C_c - \Gamma^*)}{C_c + K_{\text{mC}} \times (1 + O_c / K_{\text{mO}})}, \quad (14a)$$

$$A_J = \frac{J_p (C_c - \Gamma^*)}{4 C_c + 2\Gamma^*} \quad (14b)$$

where  $K_{\text{mC}}$  is the Michaelis–Menten constants of Rubisco for  $\text{CO}_2$  270  $\mu\text{bar}$ , [73];  $K_{\text{mO}}$  is the Michaelis–Menten constants of Rubisco for  $\text{O}_2$  16,500  $\mu\text{bar}$ , [73];  $O_c$  is the chloroplastic  $\text{O}_2$  partial pressure, assumed to equal to the oxygen partial pressure 230,000  $\mu\text{bar}$ , [74];  $J_p$  is the potential electron transport rate [47]:

$$J_p = \frac{\sigma \times \text{PAR} + J_{\text{max}} - \sqrt{(\sigma \times \text{PAR} + J_{\text{max}})^2 - 4 \times \theta \times \sigma \times \text{PAR} \times J_{\text{max}}}}{2 \times \theta}, \quad (15)$$

where  $\sigma$  is the product of leaf light absorptance, a fraction of absorbed photons allocated to PSII and  $\Phi_{P_{\max}}$ .  $\sigma$  is set to 0.3 [72].  $\theta$  is an empirical curvature parameter, which is also modelled as a function of  $\theta_{\text{SWC}}$ :

$$\theta = k \times \exp^{((-1) \times \theta_{\text{swc}})} + m, \quad (16)$$

where  $k$ ,  $l$ , and  $m$  are the fitting parameters. Again, 50% of the measurements were used to determine the parameter values by minimizing the squared difference between the measured and simulated values of  $\Phi_P$  (Table S1).

$A_{\text{net}}$  is limited by biochemical processes under water stress, such that a soil-moisture-dependent stress function ( $\beta_B$ , see Equation (22) below) should be applied to regulate the parameters  $J_{\text{max}}$  and  $V_{\text{cmax}}$  of the photosynthesis model [75]:

$$J_{\text{max}} = \beta_B \times J_{\text{max},0}, \quad (17a)$$

$$V_{\text{cmax}} = \beta_B \times V_{\text{cmax},0} \quad (17b)$$

where  $J_{\text{max},0}$  and  $V_{\text{cmax},0}$  represent the unstressed values of  $J_{\text{max}}$  and  $V_{\text{cmax}}$ , respectively, at the beginning of the experiment.

#### 4.6. Estimation of $\Gamma^*$ , $R_d$ , and $C_c$

Katul et al. [76] and Liu et al. [77] showed that  $\Gamma^*$  can be estimated as a function of  $T_{\text{air}}$ :

$$\Gamma^* = 36.9 + 1.18 \times (T_{\text{air}} - 25) + 0.036 \times (T_{\text{air}} - 25)^2, \quad (18)$$

Here, we used air temperature as measured in the LI-6800 leaf chamber.  $R_d$  is described as [78]:

$$R_d = 0.015 \times V_{\text{cmax},0}, \quad (19)$$

Mesophyll conductance to  $\text{CO}_2$  was assumed to be infinite and thus  $C_c$  was considered to be equal to intercellular  $\text{CO}_2$  partial pressure  $C_i$ , [53].  $C_i$  is estimated as [79]:

$$C_i = C_a - \frac{A_{\text{net}}}{G_c}, \quad (20)$$

where  $C_a$  is the ambient air  $\text{CO}_2$  partial pressure ( $\mu\text{mol mol}^{-1}$ ), and  $G_c$  is the stomatal conductance for  $\text{CO}_2$  ( $\text{mol m}^{-2} \text{s}^{-1}$ ).  $A_{\text{net}}$  is the minimum of  $A_C$  and  $A_J$  (Equation (14)). Because  $C_i$ ,  $A_{\text{net}}$ , and  $G_c$  are coupled to each other, the estimation of  $A_{\text{net}}$  and  $G_c$  has to be resolved iteratively over  $C_i$  given an initial value, which is  $C_i = 0.7 \times C_a$  for C3 winter wheat [80]. The iterative loop stops when the difference in  $C_i$  between two successive iterations is less than  $0.1 \mu\text{mol mol}^{-1}$ . The biochemical model of photosynthesis proposed by Farquhar, von Caemmerer and Berry [64] was used to estimate  $A_{\text{net}}$  as the minimum of the Rubisco-limited  $\text{CO}_2$  assimilation rate and the electron-transport-limited  $\text{CO}_2$  assimilation rate.

$G_c$  is estimated using a modified Ball–Woodrow–Berry model BWB [81]:

$$G_s = G_0 + \frac{a \times \beta_s \times A_{\text{net}}}{C_s \times (1 + \text{VPD}/D_0)}, \quad (21a)$$

$$G_c = 0.64 \times G_s \quad (21b)$$

where  $G_0$  is the residual conductance ( $\text{mol m}^{-2} \text{s}^{-1}$ ), assumed to be 0.01 [81];  $C_s$  is the  $\text{CO}_2$  concentration at the leaf surface ( $\mu\text{mol mol}^{-1}$ ), assumed to be the product of  $a/(a - 1)$  and  $C_i$ ; VPD is the vapor pressure deficit (kPa);  $D_0$  (kPa) is an empirical parameter related to stomatal sensitivity to VPD, assumed to be 1.5 [81];  $a$  is a parameter related to  $C_i$ , assumed to be 11.0 [81]; 0.64 is a factor used to convert the molecular diffusivity of water vapor to  $\text{CO}_2$  [79];  $\beta_s$  is the normalized soil-moisture-dependent stress function which accounts for the reduction in  $G_s$  under water stress.  $\beta_s$  and  $\beta_B$  (Equation (17)) can be defined as:

$$\beta_i = \begin{cases} 0 & \theta_{\text{SWC}} < \theta_{\text{WP}} \\ \left[ \frac{\theta_{\text{SWC}} - \theta_{\text{WP}}}{\theta_{\text{FC}} - \theta_{\text{WP}}} \right]^{q_j} & \theta_{\text{WP}} \leq \theta_{\text{SWC}} \leq \theta_{\text{FC}} \\ 1 & \theta_{\text{SWC}} > \theta_{\text{FC}} \end{cases}, \quad (22)$$

where  $\beta_i$  ranges between 1 (for plants not suffering from drought) and 0 (transpiration is zero); the subscripts  $i = B$  and  $S$  are for biochemical and stomatal limitations, respectively [75];  $\theta_{\text{FC}}$  and  $\theta_{\text{WP}}$  represent  $\theta_{\text{SWC}}$  at the field capacity (24%) and wilting point (9%); the fitting parameter  $q_j$  is a measure of the nonlinearity of the effects of water stress on the biochemical and stomatal limitations, and  $j$  takes the values  $B$  and  $S$  for  $i = B$  and  $S$ , respectively [75,82].  $q_B$  (Equation (17)) and  $q_S$  in (Equation (21)) were determined by minimizing a cost function,  $C = (M - S)^2$ , where  $M$  represents the measurement and  $S$  is the corresponding simulated value ( $V_{\text{cmax}}$  for  $q_B$ , and  $G_s$  for  $q_S$ ).

## 5. Conclusions

Our results show that the response of fluorescence emissions to drought is smaller than those of either stomatal conductance or net photosynthetic carbon assimilation. At the canopy scale and beyond, however, structural dynamics dominate the spatial variation

of canopy SIF in response to water stress, explaining the strong drought response of SIF retrieved from space. As drought becomes more severe, the shifts in energy allocation towards decreasing photochemistry and increasing fluorescence emission tend to push plants into the PQ phase, enhancing the nonlinearity in the overall relationship between photochemistry and fluorescence. We confirm that SIF alone has a limited ability to predict drought-induced declines in photosynthetic parameters. Alternatively, the rMLR model, using SIF as one important input variable, demonstrates a satisfactory performance in reproducing declines in stomatal conductance and net photosynthetic carbon assimilation. The rMLR model has good potential for applications at regional and global scales, and thus provides the basis for using SIF mechanistically to estimate GPP under the scenario of increasing intensity and the extent of droughts in the twenty-first century.

**Supplementary Materials:** The following supporting information can be downloaded at: <https://www.mdpi.com/article/10.3390/plants12193365/s1>; Notes S1: Calculation of  $\phi_P$ ,  $\phi_F$ ,  $\phi_N$ ,  $\phi_D$ , NPQ,  $\phi_{P_{max}}$  and  $J_{a\_PAM}$ ; Figure S1: Variations in  $\beta_S$  and  $\beta_B$  for the water stress (WS, diamonds) treatments under 12 days of progressive drought stress; Figure S2: Average absorbed photosynthetically active radiation (APAR,  $\mu\text{mol m}^{-2} \text{s}^{-1}$ ) under changing light intensity over the duration of the drought; Figure S3: The responses of full-band chlorophyll fluorescence emission at the photosystem level ( $\text{ChlF}_{P\_F}$ ,  $\mu\text{mol m}^{-2} \text{s}^{-1}$ ) to changing light intensity during the period between 14 and 28 days (WS14 to WS28) after withholding water; Table S1: List of retrieved parameters, their initial values, lower boundaries (LB), upper boundaries (UB) and constraints.

**Author Contributions:** Q.J. and X.L. planned and designed the research. Z.L. developed model assumptions and scenarios. Q.J., C.G., Y.W., J.Y. and J.W. performed experiments. Q.J. analyzed data. Q.J. and X.L. wrote the manuscript. Q.Y., F.Z. and X.L. edited the manuscript. All authors have read and agreed to the published version of the manuscript.

**Funding:** The research was supported by the National Natural Science Foundation of China (Grant No. 41901293 to Z.L., and 42071328 to X.L.), the China Postdoctoral Science Foundation (Grant No. 2019M663828 to Z.L.), and the Chinese Universities Scientific Fund (24520212452021125 to X.L.).

**Data Availability Statement:** The data are available on request from the authors. The data supporting the findings of this study are available from the corresponding author, Xiaoliang Lu, upon request.

**Acknowledgments:** The authors would like to thank the anonymous reviewers for their valuable comments and suggestions. The authors gratefully thank Huanlin Gao for helping with the experiment.

**Conflicts of Interest:** The authors have no conflict of interest to declare.

## Appendix A. Definitions, Symbols and Methods for the Nomenclature in This Paper

| Symbols              | Definition  | Unit                                 |
|----------------------|---|--------------------------------------|
| $J_a$                | the actual rate of electron transport calculated from ChlF emission   | $\mu\text{mol m}^{-2} \text{s}^{-1}$ |
| $q_L$                | fraction of open PSII reaction centers  | /                                    |
| $\phi_{P_{max}}$     | maximum photochemical quantum yield of PSII   | /                                    |
| $K_D$                | the rate constants for constitutive heat loss   | /                                    |
| $K_F$                | the rate constants for fluorescence   | /                                    |
| $K_{DF}$             | the ratio between ( $K_D$ ) and ( $K_F$ )   | /                                    |
| $\text{ChlF}_{P\_F}$ | chlorophyll fluorescence flux density emitted from the photosystem II (PSII) across the full ChlF emission spectrum | $\mu\text{mol m}^{-2} \text{s}^{-1}$ |
| $\phi_P$             | the quantum yields of photochemical quenching in PSII   | /                                    |
| NPQ                  | non-photochemical quenching,  | /                                    |
| PAR                  | photochemically active radiation  | $\mu\text{mol m}^{-2} \text{s}^{-1}$ |
| $T_{air}$            | air temperature   | $^{\circ}\text{C}$                   |

| Symbols                          | Definition  | Unit  |
|----------------------------------|---|---|
| $A_{\text{net}}$                 | net CO <sub>2</sub> assimilation rate   | $\mu\text{mol m}^{-2} \text{s}^{-1}$                |
| $A_{\text{g}}$                   | gross photosynthesis  | $\mu\text{mol m}^{-2} \text{s}^{-1}$                |
| $R_{\text{d}}$                   | the daytime respiration   | $\mu\text{mol m}^{-2} \text{s}^{-1}$                |
| $C_{\text{c}}$                   | the chloroplastic CO <sub>2</sub> partial pressure  | $\mu\text{mol m}^{-2} \text{s}^{-1}$                |
| $\Gamma^*$                       | the chloroplastic compensation point of CO <sub>2</sub>   | $\mu\text{mol m}^{-2} \text{s}^{-1}$                |
| $\zeta$                          | the fraction of total electron transport of mesophyll and bundle sheath allocated to mesophyll                                | /   |
| $F_1$                            | the PSI fluorescence yield by the PAM fluorometer for C <sub>3</sub> species  | /   |
| $F_0$                            | minimal fluorescence in the dark of dark-adapted leaves from the PAM  | /   |
| $F_m$                            | maximal fluorescence in the dark of dark-adapted leaves from the PAM  | /   |
| $F_m'$                           | maximal fluorescence emission in the light-adapted state from the PAM   | /   |
| $F_t$                            | steady-state fluorescence emission induced by the measuring beam of the PAM fluorometer                                       | /   |
| $\phi_F$                         | the quantum yield of fluorescence emission  | /   |
| $\phi_N$                         | the quantum yield of regulated heat dissipation   | /   |
| $\phi_D$                         | the quantum yield of constitutive heat dissipation  | /   |
| $\text{ChlF}_L(\lambda)$         | the passive ChlF spectrum in the range 640 to 850 nm at the leaf scale  | $\text{mW m}^{-2} \text{nm}^{-1} \text{sr}^{-1}$    |
| $\text{ChlF}_{L\_U}(\lambda)$    | the fluorescence radiance emitted from adaxial leaf surfaces  | $\mu\text{W cm}^{-2} \text{nm}^{-1} \text{sr}^{-1}$ |
| $\text{ChlF}_{L\_D}$             | the fluorescence radiance emitted from abaxial leaf surfaces  | $\mu\text{W cm}^{-2} \text{nm}^{-1} \text{sr}^{-1}$ |
| $\text{ChlF}_{L\_PSII}(\lambda)$ | the contribution of PSII to measurements of $\text{ChlF}_L(\lambda)$  | $\text{mW m}^{-2} \text{nm}^{-1} \text{sr}^{-1}$    |
| $F_{1\_SW}$                      | the PSI contribution at SW wavelengths, $F_{1\_SW} = 0.14 \times F_0$   | /   |
| $F_{1\_LW}$                      | the PSI contribution at LW wavelengths, $F_{1\_LW} = 0.45 \times F_0$   | /   |
| $\text{ChlF}_P(\lambda)$         | downscaling the $\text{ChlF}_{L\_PSII}(\lambda)$ to the photosystem level   | $\text{mW m}^{-2} \text{nm}^{-1} \text{sr}^{-1}$    |
| $f_{\text{esc\_P-L}}$            | the probability that a fluorescence photon escapes from the PSII light reactions inside the leaves to the surface of the leaf | /   |
| $R$                              | leaf reflectance  | /   |
| $T$                              | leaf transmittance  | /   |
| $K_N$                            | the rate coefficients of energy-dependent heat dissipation  | /   |
| $\chi$                           | the relative light saturation   | /   |
| $\theta_{\text{SWC}}$            | gravimetric soil water content  | %   |
| $A_C$                            | Rubisco-limited gross CO <sub>2</sub> assimilation  | $\mu\text{mol m}^{-2} \text{s}^{-1}$                |
| $A_J$                            | RuBP-limited gross CO <sub>2</sub> assimilation   | $\mu\text{mol m}^{-2} \text{s}^{-1}$                |
| $\alpha_{\text{grn}}$            | the absorption efficiency of PAR by green leaves  | /   |
| $\beta_{\text{PSII}}$            | fraction of absorbed energy allocated to PSII   | /   |
| $\sigma$                         | the product of leaf light absorptance, fraction of absorbed photons allocated to PSII and $\phi_{\text{Pmax}}$                | /   |
| $V_{\text{cmax}}$                | the maximum carboxylation capacity of Rubisco   | $\mu\text{mol m}^{-2} \text{s}^{-1}$                |
| $K_{\text{mC}}$                  | Michaelis–Menten constants of Rubisco for CO <sub>2</sub>   | $\mu\text{bar}$                                     |
| $K_{\text{mO}}$                  | Michaelis–Menten constants of Rubisco for O <sub>2</sub>  | $\mu\text{bar}$                                     |
| $O_{\text{c}}$                   | the chloroplastic O <sub>2</sub> partial pressure   | $\mu\text{bar}$                                     |

| Symbols              | Definition  | Unit                                 |
|----------------------|---|--------------------------------------|
| $J_p$                | the potential electron transport rate   | $\mu\text{mol m}^{-2} \text{s}^{-1}$ |
| $J_{\text{max}}$     | the maximum electron transport rate   | $\mu\text{mol m}^{-2} \text{s}^{-1}$ |
| $\beta_B$            | the soil-moisture-dependent stress function which accounts for the reduction in $V_{\text{cmax}}$ and $J_{\text{max}}$ under water stress | /                                    |
| $V_{\text{cmax},0}$  | unstressed $V_{\text{cmax}}$ at the beginning of the experiment   | $\mu\text{mol m}^{-2} \text{s}^{-1}$ |
| $J_{\text{max},0}$   | unstressed $J_{\text{max}}$ at the beginning of the experiment  | $\mu\text{mol m}^{-2} \text{s}^{-1}$ |
| $C_i$                | the intercellular $\text{CO}_2$ concentration   | $\mu\text{mol mol}^{-1}$             |
| $C_a$                | the ambient air $\text{CO}_2$ partial pressure  | $\mu\text{mol mol}^{-1}$             |
| $G_c$                | the stomatal conductance for $\text{CO}_2$  | $\text{mol m}^{-2} \text{s}^{-1}$    |
| $G_s$                | stomatal conductance to water vapor   | $\text{mol m}^{-2} \text{s}^{-1}$    |
| $G_0$                | the residual conductance  | $\text{mol mol}^{-1}$                |
| $a$                  | a parameter related to $C_i$  | /                                    |
| $\beta_S$            | the normalized soil-moisture-dependent stress function which accounts for the reduction in $G_s$ under water stress                       | /                                    |
| $C_s$                | the $\text{CO}_2$ concentration at the leaf surface   | $\mu\text{mol mol}^{-1}$             |
| VPD                  | the vapor pressure deficit  | kPa                                  |
| $D_0$                | an empirical parameter related to stomatal sensitivity to VPD   | kPa                                  |
| $q_B$                | a measure of the nonlinearity of the effects of water stress on the biochemical   | /                                    |
| $q_S$                | a measure of the nonlinearity of the effects of water stress on the stomatal limitations  | /                                    |
| $\theta_{\text{FC}}$ | $\theta_{\text{SWC}}$ at field capacity   | %                                    |
| $\theta_{\text{WP}}$ | $\theta_{\text{SWC}}$ at wilting point  | %                                    |
| $J_{\text{a\_PAM}}$  | the actual rate of electron transport from the PAM  | $\mu\text{mol m}^{-2} \text{s}^{-1}$ |
| $J_{\text{max},0}$   | unstressed $J_{\text{max}}$ at the beginning of the experiment  | $\mu\text{mol m}^{-2} \text{s}^{-1}$ |

## References

- Baker, N.R. Chlorophyll fluorescence: A probe of photosynthesis in vivo. *Annu. Rev. Plant Biol.* **2008**, *59*, 89–113. [[CrossRef](#)] [[PubMed](#)]
- Meroni, M.; Rossini, M.; Guanter, L.; Alonso, L.; Rascher, U.; Colombo, R.; Moreno, J. Remote sensing of solar-induced chlorophyll fluorescence: Review of methods and applications. *Remote Sens. Environ.* **2009**, *113*, 2037–2051. [[CrossRef](#)]
- Porcar-Castell, A.; Tyystjärvi, E.; Atherton, J.; Van der Tol, C.; Flexas, J.; Pfündel, E.E.; Moreno, J.; Frankenberg, C.; Berry, J.A. Linking chlorophyll a fluorescence to photosynthesis for remote sensing applications: Mechanisms and challenges. *J. Exp. Bot.* **2014**, *65*, 4065–4095. [[CrossRef](#)] [[PubMed](#)]
- Magney, T.S.; Frankenberg, C.; Köhler, P.; North, G.; Davis, T.S.; Dold, C.; Dutta, D.; Fisher, J.B.; Grossmann, K.; Harrington, A. Disentangling changes in the spectral shape of chlorophyll fluorescence: Implications for remote sensing of photosynthesis. *J. Geophys. Res. Biogeosci.* **2019**, *124*, 1491–1507. [[CrossRef](#)]
- Schreiber, U.; Schliwa, U.; Bilger, W. Continuous recording of photochemical and non-photochemical chlorophyll fluorescence quenching with a new type of modulation fluorometer. *Photosynth. Res.* **1986**, *10*, 51–62. [[CrossRef](#)]
- Bilger, W.; Schreiber, U.; Bock, M. Determination of the quantum efficiency of photosystem II and of non-photochemical quenching of chlorophyll fluorescence in the field. *Oecologia* **1995**, *102*, 425–432. [[CrossRef](#)]
- Govindjee, G. Sixty-three years since Kautsky: Chlorophyll a fluorescence. *Aust. J. Plant Physiol.* **1995**, *22*, 131–160. [[CrossRef](#)]
- Frankenberg, C.; O'Dell, C.; Berry, J.; Guanter, L.; Joiner, J.; Köhler, P.; Pollock, R.; Taylor, T.E. Prospects for chlorophyll fluorescence remote sensing from the orbiting carbon observatory-2. *Remote Sens. Environ.* **2014**, *147*, 1–12. [[CrossRef](#)]
- Yang, X.; Tang, J.W.; Mustard, J.F.; Lee, J.E.; Rossini, M.; Joiner, J.; Munger, J.W.; Kornfeld, A.; Richardson, A.D. Solar-induced chlorophyll fluorescence that correlates with canopy photosynthesis on diurnal and seasonal scales in a temperate deciduous forest. *Geophys. Res. Lett.* **2015**, *42*, 2977–2987. [[CrossRef](#)]
- Köhler, P.; Frankenberg, C.; Magney, T.S.; Guanter, L.; Joiner, J.; Landgraf, J. Global retrievals of solar-induced chlorophyll fluorescence with TROPOMI: First results and intersensor comparison to OCO-2. *Geophys. Res. Lett.* **2018**, *45*, 10456–10463. [[CrossRef](#)]

11. Yang, H.L.; Yang, X.; Zhang, Y.G.; Heskell, M.A.; Lu, X.L.; Munger, J.W.; Sun, S.; Tang, J.W. Chlorophyll fluorescence tracks seasonal variations of photosynthesis from leaf to canopy in a temperate forest. *Glob. Chang. Biol.* **2017**, *23*, 2874–2886. [[CrossRef](#)] [[PubMed](#)]
12. He, L.Y.; Magney, T.; Dutta, D.; Yin, Y.; Köhler, P.; Grossmann, K.; Stutz, J.; Dold, C.; Hatfield, J.; Guan, K.Y. From the ground to space: Using solar-induced chlorophyll fluorescence to estimate crop productivity. *Geophys. Res. Lett.* **2020**, *47*, e2020GL087474. [[CrossRef](#)]
13. Kimm, H.; Guan, K.; Burroughs, C.H.; Peng, B.; Ainsworth, E.A.; Bernacchi, C.J.; Moore, C.E.; Kumagai, E.; Yang, X.; Berry, J.A. Quantifying high-temperature stress on soybean canopy photosynthesis: The unique role of sun-induced chlorophyll fluorescence. *Glob. Chang. Biol.* **2021**, *27*, 2403–2415. [[CrossRef](#)]
14. Verma, M.; Schimel, D.; Evans, B.; Frankenberg, C.; Beringer, J.; Drewry, D.T.; Magney, T.; Marang, I.; Hutley, L.; Moore, C. Effect of environmental conditions on the relationship between solar-induced fluorescence and gross primary productivity at an OzFlux grassland site. *J. Geophys. Res. Biogeosci.* **2017**, *122*, 716–733. [[CrossRef](#)]
15. Sun, Y.; Frankenberg, C.; Jung, M.; Joiner, J.; Guanter, L.; Köhler, P.; Magney, T. Overview of Solar-Induced chlorophyll Fluorescence (SIF) from the Orbiting Carbon Observatory-2: Retrieval, cross-mission comparison, and global monitoring for GPP. *Remote Sens. Environ.* **2018**, *209*, 808–823. [[CrossRef](#)]
16. Marrs, J.; Reblin, J.; Logan, B.; Allen, D.; Reinmann, A.; Bombard, D.; Tabachnik, D.; Hutyrá, L. Solar-induced fluorescence does not track photosynthetic carbon assimilation following induced stomatal closure. *Geophys. Res. Lett.* **2020**, *47*, e2020GL087956. [[CrossRef](#)]
17. IPCC. *Climate Change and Land: An IPCC Special Report on Climate Change, Desertification, Land Degradation, Sustainable Land Management, Food Security, and Greenhouse Gas Fluxes in Terrestrial Ecosystems*; IPCC: Geneva, Switzerland, 2019.
18. Hanjra, M.A.; Qureshi, M.E. Global water crisis and future food security in an era of climate change. *Food Policy* **2010**, *35*, 365–377. [[CrossRef](#)]
19. Kim, W.; Iizumi, T.; Nishimori, M. Global patterns of crop production losses associated with droughts from 1983 to 2009. *J. Appl. Meteorol. Climatol.* **2019**, *58*, 1233–1244. [[CrossRef](#)]
20. Leng, G.Y.; Hall, J. Crop yield sensitivity of global major agricultural countries to droughts and the projected changes in the future. *Sci. Total Environ.* **2019**, *654*, 811–821. [[CrossRef](#)]
21. Ayaz, A.; Huang, H.; Zheng, M.; Zaman, W.; Li, D.; Saqib, S.; Zhao, H.; Lü, S. Molecular cloning and functional analysis of GmLACS2-3 reveals its involvement in cutin and suberin biosynthesis along with abiotic stress tolerance. *Int. J. Mol. Sci.* **2021**, *22*, 9175. [[CrossRef](#)] [[PubMed](#)]
22. FAO/STAT. *Food and Agriculture Organization of the United Nations—Crop Statistics on Lupin Production*; FAO/STAT: Rome, Italy, 2018.
23. Lu, C.M.; Zhang, J.H. Effects of water stress on photosystem II photochemistry and its thermostability in wheat plants. *J. Exp. Bot.* **1999**, *50*, 1199–1206. [[CrossRef](#)]
24. Hlavinka, P.; Trnka, M.; Semerádová, D.; Dubrovský, M.; Žalud, Z.; Možný, M. Effect of drought on yield variability of key crops in Czech Republic. *Agric. For. Meteorol.* **2009**, *149*, 431–442. [[CrossRef](#)]
25. Ouyang, W.J.; Struijk, P.C.; Yin, X.Y.; Yang, J.C. Stomatal conductance, mesophyll conductance, and transpiration efficiency in relation to leaf anatomy in rice and wheat genotypes under drought. *J. Exp. Bot.* **2017**, *68*, 5191–5205. [[CrossRef](#)]
26. Sun, Y.; Fu, R.; Dickinson, R.; Joiner, J.; Frankenberg, C.; Gu, L.H.; Xia, Y.L.; Fernando, N. Drought onset mechanisms revealed by satellite solar-induced chlorophyll fluorescence: Insights from two contrasting extreme events. *J. Geophys. Res. Biogeosci.* **2015**, *120*, 2427–2440. [[CrossRef](#)]
27. Yoshida, Y.; Joiner, J.; Tucker, C.; Berry, J.; Lee, J.-E.; Walker, G.; Reichle, R.; Koster, R.; Lyapustin, A.; Wang, Y. The 2010 Russian drought impact on satellite measurements of solar-induced chlorophyll fluorescence: Insights from modeling and comparisons with parameters derived from satellite reflectances. *Remote Sens. Environ.* **2015**, *166*, 163–177. [[CrossRef](#)]
28. Xu, S.; Atherton, J.; Riikonen, A.; Zhang, C.; Oivukkamäki, J.; MacArthur, A.; Honkavaara, E.; Hakala, T.; Koivumäki, N.; Liu, Z.G. Structural and photosynthetic dynamics mediate the response of SIF to water stress in a potato crop. *Remote Sens. Environ.* **2021**, *263*, 112555. [[CrossRef](#)]
29. Helm, L.T.; Shi, H.Y.; Lerdau, M.T.; Yang, X. Solar-induced chlorophyll fluorescence and short-term photosynthetic response to drought. *Ecol. Appl.* **2020**, *30*, e02101. [[CrossRef](#)]
30. Magney, T.S.; Barnes, M.L.; Yang, X. On the covariation of chlorophyll fluorescence and photosynthesis across scales. *Geophys. Res. Lett.* **2020**, *47*, e2020GL091098. [[CrossRef](#)]
31. Gu, L.H.; Han, J.M.; Wood, J.D.; Chang, C.Y.Y.; Sun, Y. Sun-induced Chl fluorescence and its importance for biophysical modeling of photosynthesis based on light reactions. *New Phytol.* **2019**, *223*, 1179–1191. [[CrossRef](#)]
32. van der Tol, C.; Berry, J.; Campbell, P.; Rascher, U. Models of fluorescence and photosynthesis for interpreting measurements of solar-induced chlorophyll fluorescence. *J. Geophys. Res. Biogeosci.* **2014**, *119*, 2312–2327. [[CrossRef](#)]
33. Damm, A.; Guanter, L.; Paul-Limoges, E.; Van der Tol, C.; Hueni, A.; Buchmann, N.; Eugster, W.; Ammann, C.; Schaepman, M.E. Far-red sun-induced chlorophyll fluorescence shows ecosystem-specific relationships to gross primary production: An assessment based on observational and modeling approaches. *Remote Sens. Environ.* **2015**, *166*, 91–105. [[CrossRef](#)]
34. Maguire, A.J.; Eitel, J.U.; Griffin, K.L.; Magney, T.S.; Long, R.A.; Vierling, L.A.; Schmiede, S.C.; Jennewein, J.S.; Weygint, W.A.; Boelman, N.T. On the functional relationship between fluorescence and photochemical yields in complex evergreen needleleaf canopies. *Geophys. Res. Lett.* **2020**, *47*, e2020GL087858. [[CrossRef](#)]

35. Chen, X.J.; Mo, X.G.; Hu, S.; Liu, S.X. Relationship between fluorescence yield and photochemical yield under water stress and intermediate light conditions. *J. Exp. Bot.* **2019**, *70*, 301–313. [[CrossRef](#)] [[PubMed](#)]
36. Faraloni, C.; Cutino, I.; Petruccioli, R.; Leva, A.R.; Lazzeri, S.; Torzillo, G. Chlorophyll fluorescence technique as a rapid tool for in vitro screening of olive cultivars (*Olea europaea* L.) tolerant to drought stress. *Environ. Exp. Bot.* **2011**, *73*, 49–56. [[CrossRef](#)]
37. Jiang, Y.; Ye, J.; Niinemets, Ü. Dose-dependent methyl jasmonate effects on photosynthetic traits and volatile emissions: Biphasic kinetics and stomatal regulation. *Plant Signal. Behav.* **2021**, *16*, 1917169. [[CrossRef](#)]
38. Jiang, Y.; Ye, J.; Rasulov, B.; Niinemets, Ü. Role of stomatal conductance in modifying the dose response of stress-volatile emissions in methyl jasmonate treated leaves of cucumber (*Cucumis sativa*). *Int. J. Mol. Sci.* **2020**, *21*, 1018. [[CrossRef](#)]
39. Yamashita, F.; Rodrigues, A.L.; Rodrigues, T.M.; Palermo, F.H.; Baluška, F.; de Almeida, L.F.R. Potential plant–plant communication induced by infochemical methyl jasmonate in sorghum (*Sorghum bicolor*). *Plants* **2021**, *10*, 485. [[CrossRef](#)] [[PubMed](#)]
40. Muller, P.; Li, X.P.; Niyogi, K.K. Non-photochemical quenching. A response to excess light energy. *Plant Physiol.* **2001**, *125*, 1558–1566. [[CrossRef](#)] [[PubMed](#)]
41. Flexas, J.; Medrano, H. Drought-inhibition of photosynthesis in C3 plants: Stomatal and non-stomatal limitations revisited. *Ann. Bot.* **2002**, *89*, 183–189. [[CrossRef](#)]
42. Adams, W.W.; Zarter, C.R.; Ebbert, V.; Demmig-Adams, B. Photoprotective strategies of overwintering evergreens. *Bioscience* **2004**, *54*, 41–49. [[CrossRef](#)]
43. Verhoeven, A. Sustained energy dissipation in winter evergreens. *New Phytol.* **2013**, *201*, 57–65. [[CrossRef](#)]
44. Porcar-Castell, A.; Malenovsky, Z.; Magney, T.; Van Wittenberghe, S.; Fernández-Marín, B.; Maignan, F.; Zhang, Y.G.; Maseyk, K.; Atherton, J.; Albert, L.P. Chlorophyll a fluorescence illuminates a path connecting plant molecular biology to earth-system science. *Nat. Plants* **2021**, *7*, 998–1009. [[CrossRef](#)] [[PubMed](#)]
45. Sloat, L.L.; Lin, M.; Butler, E.E.; Johnson, D.; Holbrook, N.M.; Huybers, P.J.; Lee, J.-E.; Mueller, N.D. Evaluating the benefits of chlorophyll fluorescence for in-season crop productivity forecasting. *Remote Sens. Environ.* **2021**, *260*, 112478. [[CrossRef](#)]
46. Liu, Z.Q.; Zhao, F.; Liu, X.J.; Yu, Q.; Wang, Y.F.; Peng, X.B.; Cai, H.J.; Lu, X.L. Direct estimation of photosynthetic CO<sub>2</sub> assimilation from solar-induced chlorophyll fluorescence (SIF). *Remote Sens. Environ.* **2022**, *271*, 112893. [[CrossRef](#)]
47. Han, J.M.; Chang, C.Y.Y.; Gu, L.H.; Zhang, Y.J.; Meeker, E.W.; Magney, T.S.; Walker, A.P.; Wen, J.M.; Kira, O.; McNaull, S.; et al. The physiological basis for estimating photosynthesis from chlorophyll a fluorescence. *New Phytol.* **2022**, *234*, 120–1219. [[CrossRef](#)] [[PubMed](#)]
48. Bacour, C.; Maignan, F.; MacBean, N.; Porcar-Castell, A.; Flexas, J.; Frankenberg, C.; Peylin, P.; Chevallier, F.; Vuichard, N.; Bastrikov, V. Improving estimates of gross primary productivity by assimilating solar-induced fluorescence satellite retrievals in a terrestrial biosphere model using a process-based SIF model. *J. Geophys. Res. Biogeosci.* **2019**, *124*, 3281–3306. [[CrossRef](#)]
49. Zeng, Y.L.; Badgley, G.; Dechant, B.; Ryu, Y.; Chen, M.; Berry, J.A. A practical approach for estimating the escape ratio of near-infrared solar-induced chlorophyll fluorescence. *Remote Sens. Environ.* **2019**, *232*, 111209. [[CrossRef](#)]
50. Lu, X.L.; Liu, Z.Q.; Zhao, F.; Tang, J.W. Comparison of total emitted solar-induced chlorophyll fluorescence (SIF) and top-of-canopy (TOC) SIF in estimating photosynthesis. *Remote Sens. Environ.* **2020**, *251*, 112083. [[CrossRef](#)]
51. Zhao, F.; Guo, Y.Q.; Verhoef, W.; Gu, X.F.; Liu, L.Y.; Yang, G.J. A method to reconstruct the solar-induced canopy fluorescence spectrum from hyperspectral measurements. *Remote Sens.* **2014**, *6*, 10171–10192. [[CrossRef](#)]
52. Zhao, F.; Li, R.; Verhoef, W.; Cogliati, S.; Liu, X.J.; Huang, Y.B.; Guo, Y.Q.; Huang, J.X. Reconstruction of the full spectrum of solar-induced chlorophyll fluorescence: Intercomparison study for a novel method. *Remote Sens. Environ.* **2018**, *219*, 233–246. [[CrossRef](#)]
53. van der Tol, C.; Verhoef, W.; Rosema, A. A model for chlorophyll fluorescence and photosynthesis at leaf scale. *Agric. For. Meteorol.* **2009**, *149*, 96–105. [[CrossRef](#)]
54. Mohammed, G.H.; Colombo, R.; Middleton, E.M.; Rascher, U.; van der Tol, C.; Nedbal, L.; Goulas, Y.; Pérez-Priego, O.; Damm, A.; Meroni, M. Remote sensing of solar-induced chlorophyll fluorescence (SIF) in vegetation: 50 years of progress. *Remote Sens. Environ.* **2019**, *231*, 111177. [[CrossRef](#)]
55. Rodell, M.; Houser, P.R.; Jambor, U.; Gottschalck, J.; Mitchell, K.; Meng, C.-J.; Arsenault, K.; Cosgrove, B.; Radakovich, J.; Bosilovich, M. The global land data assimilation system. *Bull. Am. Meteorol. Soc.* **2004**, *85*, 381–394. [[CrossRef](#)]
56. Reichle, R.H.; Liu, Q.; Koster, R.D.; Crow, W.T.; De Lannoy, G.J.; Kimball, J.S.; Ardizzone, J.V.; Bosch, D.; Colliander, A.; Cosh, M. Version 4 of the SMAP Level-4 soil moisture algorithm and data product. *J. Adv. Model. Earth Syst.* **2019**, *11*, 3106–3130. [[CrossRef](#)]
57. Meeker, E.W.; Magney, T.S.; Bambach, N.; Momayyezi, M.; McElrone, A.J. Modification of a gas exchange system to measure active and passive chlorophyll fluorescence simultaneously under field conditions. *AoB Plants* **2021**, *13*, plaa066. [[CrossRef](#)] [[PubMed](#)]
58. Chen, Y.G.; Chen, F.Q.; Liu, L.; Zhu, S.B. Physiological responses of *Leucaena leucocephala* seedlings to drought stress. *Procedia Eng.* **2012**, *28*, 110–116.
59. Wei, Y.Q.; Jin, J.L.; Jiang, S.M.; Ning, S.W.; Liu, L. Quantitative response of soybean development and yield to drought stress during different growth stages in the Huaibei Plain, China. *Agronomy* **2018**, *8*, 97. [[CrossRef](#)]
60. Li, F.S.; Liang, J.H.; Kang, S.Z.; Zhang, J.H. Benefits of alternate partial root-zone irrigation on growth, water and nitrogen use efficiencies modified by fertilization and soil water status in maize. *Plant Soil* **2007**, *295*, 279–291. [[CrossRef](#)]
61. Arzanesh, M.H.; Alikhani, H.A.; Khavazi, K.; Rahimian, H.A.; Miransari, M. Wheat (*Triticum aestivum* L.) growth enhancement by *Azospirillum* sp. under drought stress. *World J. Microbiol. Biotechnol.* **2011**, *27*, 197–205. [[CrossRef](#)]

62. Dossa, K.; Diouf, D.; Cissé, N. Genome-wide investigation of Hsf genes in sesame reveals their segmental duplication expansion and their active role in drought stress response. *Front. Plant Sci.* **2016**, *7*, 1522. [[CrossRef](#)]
63. Kramer, D.M.; Johnson, G.; Kiirats, O.; Edwards, G.E. New fluorescence parameters for the determination of QA redox state and excitation energy fluxes. *Photosynth. Res.* **2004**, *79*, 209–218. [[CrossRef](#)]
64. Farquhar, G.D.; von Caemmerer, S.; Berry, J.A. A biochemical model of photosynthetic CO<sub>2</sub> assimilation in leaves of C<sub>3</sub> species. *Planta* **1980**, *149*, 78–90. [[CrossRef](#)] [[PubMed](#)]
65. Long, S.P.; Bernacchi, C. Gas exchange measurements, what can they tell us about the underlying limitations to photosynthesis? Procedures and sources of error. *J. Exp. Bot.* **2003**, *54*, 2393–2401. [[CrossRef](#)] [[PubMed](#)]
66. von Caemmerer, S. *Biochemical Models of Leaf Photosynthesis*; CSIRO Publishing: Collingwood, ON, Canada, 2000.
67. Pfündel, E.E.; Klughammer, C.; Meister, A.; Cerovic, Z.G. Deriving fluorometer-specific values of relative PSI fluorescence intensity from quenching of F<sub>0</sub> fluorescence in leaves of *Arabidopsis thaliana* and *Zea mays*. *Photosynth. Res.* **2013**, *114*, 189–206. [[CrossRef](#)] [[PubMed](#)]
68. Moya, I.; Camenen, L.; Evain, S.; Goulas, Y.; Cerovic, Z.G.; Latouche, G.; Flexas, J.; Ounis, A. A new instrument for passive remote sensing: 1. measurements of sunlight-induced chlorophyll fluorescence. *Remote Sens. Environ.* **2004**, *91*, 186–197. [[CrossRef](#)]
69. Magney, T.S.; Frankenberger, C.; Fisher, J.B.; Sun, Y.; North, G.B.; Davis, T.S.; Kornfeld, A.; Siebke, K. Connecting active to passive fluorescence with photosynthesis: A method for evaluating remote sensing measurements of Chl fluorescence. *New Phytol.* **2017**, *215*, 1594–1608. [[CrossRef](#)]
70. Pfündel, E.E. Simultaneously measuring pulse-amplitude-modulated (PAM) chlorophyll fluorescence of leaves at wavelengths shorter and longer than 700 nm. *Photosynth. Res.* **2021**, *147*, 345–358. [[CrossRef](#)] [[PubMed](#)]
71. Liu, X.J.; Liu, L.Y.; Hu, J.C.; Guo, J.; Du, S.S. Improving the potential of red SIF for estimating GPP by downscaling from the canopy level to the photosystem level. *Agric. For. Meteorol.* **2020**, *281*, 107846. [[CrossRef](#)]
72. Long, S.P.; Postl, W.; Bolhar-Nordenkamp, H.R. Quantum yields for uptake of carbon dioxide in C<sub>3</sub> vascular plants of contrasting habitats and taxonomic groupings. *Planta* **1993**, *189*, 226–234. [[CrossRef](#)]
73. Yin, X.; Struik, P.C. C<sub>3</sub> and C<sub>4</sub> photosynthesis models: An overview from the perspective of crop modelling. *NJAS-Wagening. J. Life Sci.* **2009**, *57*, 27–38. [[CrossRef](#)]
74. Wu, A.; Doherty, A.; Farquhar, G.D.; Hammer, G.L. Simulating daily field crop canopy photosynthesis: An integrated software package. *Funct. Plant Biol.* **2017**, *45*, 362–377. [[CrossRef](#)] [[PubMed](#)]
75. Egea, G.; Verhoef, A.; Vidale, P.L. Towards an improved and more flexible representation of water stress in coupled photosynthesis-stomatal conductance models. *Agric. For. Meteorol.* **2011**, *151*, 1370–1384. [[CrossRef](#)]
76. Katul, G.; Manzoni, S.; Palmroth, S.; Oren, R. A stomatal optimization theory to describe the effects of atmospheric CO<sub>2</sub> on leaf photosynthesis and transpiration. *Ann. Bot.* **2010**, *105*, 431–442. [[CrossRef](#)]
77. Liu, Y.L.; Parolari, A.J.; Kumar, M.; Huang, C.W.; Katul, G.G.; Porporato, A. Increasing atmospheric humidity and CO<sub>2</sub> concentration alleviate forest mortality risk. *Proc. Natl. Acad. Sci. USA* **2017**, *114*, 9918–9923. [[CrossRef](#)] [[PubMed](#)]
78. Collatz, G.J.; Ball, J.T.; Grivet, C.; Berry, J.A. Physiological and environmental regulation of stomatal conductance, photosynthesis and transpiration: A model that includes a laminar boundary layer. *Agric. For. Meteorol.* **1991**, *54*, 107–136. [[CrossRef](#)]
79. Ju, W.M.; Chen, J.M.; Black, T.A.; Barr, A.G.; Liu, J.; Chen, B.Z. Modelling multi-year coupled carbon and water fluxes in a boreal aspen forest. *Agric. For. Meteorol.* **2006**, *140*, 136–151. [[CrossRef](#)]
80. Wu, A.; Hammer, G.L.; Doherty, A.; von Caemmerer, S.; Farquhar, G.D. Quantifying impacts of enhancing photosynthesis on crop yield. *Nat. Plants* **2019**, *5*, 380–388. [[CrossRef](#)]
81. Wang, Y.P.; Leuning, R. A two-leaf model for canopy conductance, photosynthesis and partitioning of available energy I: Model description and comparison with a multi-layered model. *Agric. For. Meteorol.* **1998**, *91*, 89–111. [[CrossRef](#)]
82. Porporato, A.; Laio, F.; Ridolfi, L.; Rodriguez-Iturbe, I. Plants in water-controlled ecosystems: Active role in hydrologic processes and response to water stress: III. Vegetation water stress. *Adv. Water Resour.* **2001**, *24*, 725–744. [[CrossRef](#)]

**Disclaimer/Publisher’s Note:** The statements, opinions and data contained in all publications are solely those of the individual author(s) and contributor(s) and not of MDPI and/or the editor(s). MDPI and/or the editor(s) disclaim responsibility for any injury to people or property resulting from any ideas, methods, instructions or products referred to in the content.